Experimental investigation of turbulent boundary layers at high Reynolds number with uniform blowing, part I: statistics

G. Hasanuzzaman, S. Merbold, C. Cuvier, V. Motuz, J.-M. Foucaut, Ch. Egbers

THIS DRAFT WAS PREPARED USING THE LATEX STYLE FILE BELONGING TO THE JOURNAL OF TURBULENCE

Experimental investigation of turbulent boundary layers at high Reynolds number with uniform blowing, Part I: Statistics

G. Hasanuzzaman[a], S. Merbold[a]

, C. Cuvier[b], V. Motuz[a], Ch. Egbers[a] and J. -M. Foucaut[b]
[a]Department of Aerodynamics and Fluid Mechanics, Brandenburg University of Technology Cottbus-Senftenberg, Siemens-Halske-Ring-14, 03046, Cottbus, Germany;
[b]Univ. Lille, CNRS, ONERA, Arts et Metiers ParisTech, Centrale Lille, FRE 2017 - LMFL - Laboratoire de Mécanique des fluides de Lille - Kampé de Feriet, F-59000 Lille, France

ARTICLE HISTORY
Compiled January 29, 2020

ABSTRACT

Uniform blowing in wall bounded shear flows is well known for its drag reducing effects and has long been investigated ever since. However, many contemporary and former research on the present topic has confirmed the drag reducing effect but very less is known regarding how blowing mechanism is effecting the coherent structures, more importantly, their influence on the Reynolds stresses at high Reynolds number. Therefore, effect of uniform blowing has been experimentally investigated in a zero pressure gradient turbulent boundary layer (TBL). The wind tunnel used for the measurement was particularly suitable to obtain high resolution data (Boundary layer thickness[1], $\delta > 0.24m$) at high Reynolds number with Stereo Particle Image Velocimetry (SPIV) measurements. The data presented in this literature covers a large range of high Reynolds number flow e.g. $Re_\theta = 7500 \sim 19763$ where Reynolds number is based on the momentum thickness. Upstream effect of blowing was varied from $1\% \sim 6\%$ of free stream velocity by tuning the flow rate of the compressed air and measurements were taken downstream after a short interval. In order to access statistics and turbulence properties of the TBL with focus on the logarithmic and outer region, the streamwise SPIV plane (Vertical plane parallel to flow direction) configuration was used to obtain velocity fields.

KEYWORDS
Turbulent boundary layers, drag reduction, flow control, Particle Image Velocimetry, uniform blowing.

1. Introduction

In recent years, much emphasize has been given in the research of different flow control techniques for fluid driven high speed transportation e.g. air planes, ocean vessels, modern high speed trains and automobiles. Primary focus is towards the drag reduction as a consequence of surface friction. In United States alone, 40% drag is coming

CONTACT G. Hasanuzzaman. Email: hasangaz@b-tu.de

[1]Boundary layer thickness, δ is the distance from wall where mean streamwise velocity reaches 99% of free stream velocity

from skin friction in transportation sector whereas for a subsonic long range passenger liner, approximately 50% of the total drag is contributed from friction (Wood , 2004). Driven by the effort to reduce CO_2 and other Green House Gas (GHG) emission and rising fuel price, different flow control optimization techniques has been developed since the middle of 20^{th} century. Since 1950's, air transportation volume has exponentially increased, where subsonic passenger liners are the major fuel consumer (Banister et al. , 2011). Recent data indicate that shipping and airlines industry has spent $128 billion ($60/barrel (IMO , 2015)) and $130 billion ($54.2/barrel (IATA , 2017)) respectively as fuel cost. During 2018, Airline industry was estimated to spent $156 billion for fuel cost. Considering the airline cost involved in fuel expenditure, smallest saving of fuel cost determines the success/failure of the drag reduction method.

It is implausible to shift from the trend to avoid fossil fuel dependence, atleast for a foreseeable future. In order to keep the net emission at the same level from the year of 2020. International Civil Aviation Organization (ICAO) has declared a steadfast objective to improve fuel efficiency by a constant rate of 2% until 2050. In this context, an ardent challenge has been set by Airbus to reduce fuel consumption in the order of 50% within the year of 2020. Therefore, these objectives are only possible by reducing 30 - 50% of the friction drag (Kornilov , 2015). Relative financial saving by reducing drag was studied by Gad-el-Hak (1996), where a mere 10% total drag reduction of an aircraft can saves upto $ 1 billion of the annual fuel cost for the commercial airliners in USA. Under such circumstances, finding effective means to reduce friction drag is evident.

2. Flow Control Technology

In order to distinguish between the surface boundary condition, TBL over smooth surface will be denoted as Standard Boundary Layer (SBL) hereafter. Different Flow Control Techniques (FCT) which are widely investigated and have good potential to be used in wall bounded shear flows will be discussed in this section. Flow control is a term used in the field of fluid mechanics that has a predetermined range of interpretation. Generally, this refers to any mechanism applied in the flow field in order to achieve a desired alteration with a controlled outcome. With a subtle classification of the term flow control, this may be also referred as control theory and application of systems to the Navier-Stokes equations. In broader perspective, different flow control schemes can be classified into the classes of active and passive flow control which is based on their use of external energy in the control mechanism (Active: where use of external energy is required; Passive: external energy is not required).

Large part of the fuselage, wing, tail wing and radar section of a subsonic aircraft has the potential to deploy drag reduction mechanisms. Due to their size and operating speeds, the majority of commercial and military aircraft in service today are dominated by flows that results from the presence of turbulent boundary layer. This generally cover the most of the aircraft's surface. It is well known that TBL significantly increases the skin friction drag penalties when compared to laminar boundary layers. Moreover, they do result in a reduced susceptibility to flow separation due to their robustness to surface imperfections. Therefore, turbulent drag reduction has a direct relationship to the eddy structures of different size and scales present in the boundary layer.

Classical inner and outer cycle theory proposes that the effect of turbulence generation mechanism is independent of each other. Based on the fact that maximum production of turbulence occurs at approximately $11 \sim 12+$, inner cycle of turbulence

process was believed to be independent from the outer cycle, so as the structures that are generated and evolved within the inner layer was also believed to be independent from the impact of the Large Scale Motions (LSM) and Very Large Scale Motions (VLSM) from the outer layer (Kim et al. (2011)). Here, the term 'LSM' indicate the turbulent structures that are comparable to the outer scale such as boundary layer thickness (δ).

Until recently, experimental results at sufficiently high Reynolds number showed that bulk production is mostly contributed from the log layer (Smits et al. (2011)). Moreover, It is the overlapping region which is responsible for growing influence on the near wall structures at high Reynolds number. The dynamics of the inner and outer region structures are dependent on the outer region (more specifically the overlapping region) at sufficiently high Reynolds number ($Re_\theta \geq 2000$)Mathis et al. (2009). Recent insight regarding the studies of bounded shear flows have indicated that there is a significant relationship between the Turbulent Kinetic Energy (TKE) and Reynolds Shear Stress (RSS) to the large scale motions. $40 \sim 65\%$ TKE and $30 \sim 50\%$ of RSS is the contribution of large coherent eddies (¡3δ) Balakumar and Adrian (2007). Therefore, any control mechanism affecting the log region will have an upper hand over the control issue such as blowing, albeit with the cost of external energy.

Different passive control techniques worth mentioning are Super Hydrophobic Surfaces (SHS), Riblets, Large Eddy Break-up (LEBU) devices and vortex generators. Among active methods Laminar Flow Control (LFC), Uniform Continuous Blowing (UCB), Opposition Control (Blowing Only Opposition Control (BOOC)), Streamwise vortex jet flow actuators, Surfactants agent (Hellsten (2002) and Tamano et al. (2010)), Bubble Gas Injection and Transverse Standing Waves/ Vibrators.

A brief description of different methods is required in order to develop a robust flow control method. Although it is not the scope of this literature to cover all the flow control techniques in practice. Therefore, most promising ones will be highlighted based on the literature review. Some control methods are based on the type of application and working fluid, thereby, selected ones for aerodynamic applications are stressed in the following text.

2.1. Laminar Flow Control

One of the outstanding technique is LFC which was started developing since 1930s and was being developed for next 70 years subsequently. This falls within the category of active flow control technique utilized in aviation industry in order to maintain laminar state of the flow at chord Reynolds numbers beyond which the flow will normally be considered as being transitional/turbulent in the absence of control. Relaminarization of a turbulent flow state is not same as the laminar flow control. Therefore, it is often misinterpreted as a 'relaminarization' process although both flow physics phenomena may apply the same control system. Depending on the type of surfaces of a flying body (fuselage, wings etc.) such control mechanism may be applied principally in two different ways. In a way the 'Natural Laminar Flow' (NLF) is applied by creating an artificial favorable pressure gradient over the surface to delay the natural transition process to turbulent zone. Most often NLF fails to achieve a required performance for drag reduction due to the formation of inherent boundary layer instabilities. In order to overcome the limitations of LFC, a 'Hybrid Laminar Flow Concept' (HLFC) was introduced in order to reduce the suction requirements in a wide area of control surface and therefore, can reduce the system complexity by applying suction only in

the narrow region of the leading edge of the wing. Despite significant challenges, HLFC technology is in the most matured state of development.

Real scale flight test from Airbus A320 transport aircraft in 1998 was found aerodynamically successful, where micro-perforated surface was used to implement Hybrid Laminar Flow Control (HLFC) through uniform continuous suction. However, from structural point of view, suction surface required further development for simplification. Therefore, subsequent flight test in 2017 using an Airbus A340-300 (Airbus Press Release Airbus press release (2020)), which included HLFC through perforated surface not only limited to the tail leading edge but also to the wing leading edge. These are the current development for active flow control techniques using perforated surface and exhibit the readiness of the Technique. However, NLF and HLFC both present difficulty in maintaining at high Reynolds number and are subjected to the manufacturing imperfections such as waviness, roughness, joints, leading edge grits/debris strikes and discontinuities which may bring the transition points forward. Additionally, long term use of perforated surface for suction may have insect contamination and will cause financial penalties from the maintenance perspective (Choi et al. (2011)). In order to get the detailed view on the topic, Joslin (1998), Brasslow (1999), Bushnell (2003) and Reneaux (2004) are advised for interested readers.

2.2. Large Eddy Break-up Devices

One of the burning issue regarding the evaluation of a particular flow control technique in SBL is the extent of the effected region both in vertical and longitudinal direction. With increasing Reynolds number, a persistent effect is desired when control is applied. Therefore, one of the simplest way to effect the large structures beyond the viscous sub-layer is a parallel plate placed upstream. This is done in order to break the large eddy structures and to achieve a desired drag reduction effect simultaneously.

Parallel plate manipulator for the larger eddies are also known as 'Large Eddy Break-up Device' (LEBU) or parallel plate manipulator. Preliminary results from Corke et al. (1981) using Hot Wire Anemometry (HWA) measurements exhibit the damping of streamwise velocity fluctuation. Measurements taken at considerably low Reynolds number displayed persistent effect upto 70δ. Their experiment was found very effective to inhibit the intermittent large-scale structures of the SBL. Although they did not confirmed a net reduction of the skin friction. Later, Direct Numerical Simulation results from Spalart et al. (2006) rejects the idea of LEBU using for aerodynamic surfaces. Although, their finding was very interesting as LEBU devices can effectively break-up the larger eddies into smaller ones but streamwise turbulence production is very quickly recovered as opposed by the findings from Corke et al. (1981). Recently, Chin et al. (2017) performed Large Eddy Simulation (LES) of a spatially developed zero-pressure-gradient TBL within the range of $Re_\theta = 500 \sim 4300$. Persisting effect of LEBU devices were found to be active upto 160δ downstream, velocity deficit of the wake region downstream of a LEBU diminishes gradually with streamwise distance. Similar to the study from Corke et al. (1981), results from Anders (1989), Spalart et al. (2006) and Chin et al. (2017), no net reduction of friction drag was confirmed. Therefore, further literature survey on the method have shown very little/no net reduction of the skin friction drag so far.

2.3. Riblets

In a different approach that was first introduced by Liu et al. (1966), later followed by several other investigation such as Vukoslavčević et al. (1991), García-Mayoral and Jimenéz (2011) and very recently by Spallart and McLean (2011)). Riblets are similar to rough walls, is a surface of grooves aligned to the mean flow direction. Though it requires no external energy but increases the wetted surface to planform area ratio and subjected to re-installation every 5 years. Thus, such FCT is not economically feasible with a maximum of 15% of friction drag reduction.

2.4. Other techniques

Several other control techniques that are extensively studied to control SBL are jet actuators (Choi et al. (2011), Choi et al. (2011) and Mahfoze and Leizet (2017)), Opposition control (Kim et al. (2003), Stroh et al. (2015) and Abbassi et al. (2017)), Microelectromechanical systems (MEMS) (Kasagi et al., 2009), Polymer additives (White and Mungal (2008) and Benzi (2010)) and gas microbubbles (Legner (1984) and Merkle and Deutsch (1989)) were found with positive outcomes. More recently blended wing body (BWB) (Ko et al., 2003) and boundary layer ingestion (BLI) (Smith ET AL: (1993) and Plas et al. (2007)) are attractive concepts presently under investigation in aviation industry.

Among all control methods, blowing with air or other gases with different viscosities has the potential to alleviate surface friction in access of 50 % (Hwang , 2004). Therefore, within the context of this paper, we will focus on the experimental investigation of the uniform blowing as a mean to Turbulent Drag Reduction (TDR) and thereafter, its consequence on the turbulent boundary layer.

Reduction of drag is one of the principle factors that is directly influencing aircraft efficiency which is also in turn, enhance the range, speed and payload, reduce operating cost and GHG emission. Other factors such as aircraft engine and shape has been significantly optimized for last decades but much can be done in order to reduce the drag. In fact, skin friction reduction within incompressible shear flows is considered a major "Barrier problem" to the further optimization of the most aerodynamic and hydrodynamics bodies (Bushnell et al. , 1983). Classical aerodynamics conveniently segregated the total drag into pressure or form drag that include interference and roughness drag, lift drag, compressibility drag and drag due to viscosity which is also known as skin friction drag. Thereby, based on the extent of boundary layer over a subsonic aircraft, now we know that laminar region is considerably smaller than the turbulent region. Therefore, exploring viscous drag reduction in and around turbulent zone is one of the major opportunity where substantial reduction will effect the net drag contribution. Eventually, this will lead towards the overall fuel savings.

3. Flow Control Experiment in Turbulent Boundary Layer

Regarding TBL experiments one can assume that the following boundary layer is generated over flat, smooth, solid and stationary wall, hence undisturbed since transition. This states the general boundary condition for SBL. On the other hand, assumptions regarding the fluid (air) state is considered with constant density, single phase and with no external force fields. Thus only the "canonical" SBL has been investigated while manipulated using uniform blowing.

When the boundary layer is turbulent, there exist a flow where fluctuation of the velocity components are three dimensional and where occurs continuous diffusion process, production and dissipation of turbulence near the wall. Classical inner and outer cycle theory accepts that the effect of turbulence is mainly localise in the inner layer near to the wall.

SBL consists of inner and outer regions where inner region near the wall is devided into three layers. The layer adjacent to the wall is dominated by molecular viscosity and therefore also known as the viscous sub-layer. Time averaged streamwise velocity from the viscous sub-layer exhibit a linear behavior when plotted against the vertical distance from the wall. Due to the linear behavior, this is often termed as the laminar sub-layer, although evidences from several literature has showed that velocity fluctuations can also cause localized outward "Jets" (Grant (1958)). On the other hand, transport process in outer part of the inner region is dominated by turbulence, therefore effect of viscosity is neglected here. Moreover, time averaged streamwise velocity follows a logarithmic profile (Equation-6) when plotted against wall distance and commonly termed as logarithmic layer, often overlapping region. There exist a buffer layer in between logarithmic and laminar sub-layer where both modes of transport are of comparable magnitude. In order to express the extent of these layers one can use viscous length scale expressed as $l^+ = \nu/u_\tau$ (see footnote[2]). This inner layer scaling is often found very effective in order to express the general characteristics of the inner region.

4. Uniform blowing

Extensive study of SBL through DNS and LES from Kametani and Fukagata (2011) and Kametani et al. (2015) respectively has presented some very interesting results on SBL using blowing and suction. A controlled region with uniform blowing (F = 0.1, 0.5 and 1% of U_∞) and suction was applied for spatially developed SBL at momentum thickness Reynolds number $\mathrm{Re}_{\theta,SBL} = 530$ and 700. In terms of turbulence fluctuation for all three components of the velocity, magnitude was increased and significant modification along the wall was observed when uniform blowing was applied in addition to an effective skin friction drag reduction. In this aspect FIK decomposition (Fukagata et al. (2002)) of the friction drag indicate that ratio of mean convection term to the RSS term could be a good indication of the drag reduction.

In addition, outward shifting of outer peak location was observed for both Reynolds stresses and spectra. Outer and inner region peak for Reynolds stresses are enhanced as blowing magnitude increases indicates more momentum loss. On the contrary, blowing reduces the drag and enhance the turbulent spots visualized through instantaneous iso-surfaces of the flow field. As an outcome to the mean properties, δ, momentum thickness and shape factor (H) increases. Outer peak for the turbulence spectra is shifted outward. They have suggested that the rate of skin friction drag reduction through blowing at the same nominal values of blowing ratio could be higher at higher Reynolds number. Yet no data is available to support this assumption till date. However, a complete description for the statistical properties such as Reynolds number dependence of the Reynolds stresses and production is also required.

[2]In the following description of notations used with $(.)^+$ are for the parameters normalized with the wall shear velocity (u_τ) and corresponding kinematic viscosity (ν). Here, subscript $(.)_{SBL}$ indicate measurements over the smooth surface. On the other hand $(.)^*$ are the parameters normalized with the corresponding outer scale factors namely free stream velocity, U_∞ and δ.

Kametani et al. (2015) reports numerical study on spatially developing SBL with uniform blowing and suction using LES at $\mathrm{Re}_\theta = 2500$. Spatial development of the SBL exhibit greater increment of the momentum thickness and Shape factor (H) when compared to the SBL cases, this also lead to the assumption that blowing may cause flow separation if increased in magnitude. In order to validate such assumption, blowing magnitude for the present study was gradually increased upto 6%. This was attempted in order to investigate the maximum level of blowing amplitude which can sustain and stay confined within the extent of log layer. Details of the SBL mean properties are discussed in Section-7.

In addition to the turbulence statistics and mean properties of SBL flow using uniform blowing, an extensive spanwise spectral analysis of $k_z\Phi_{u'u'}$ indicate that the energy is increased for large scale structures when blowing is applied. Moreover, variation of the near wall peak is less influenced where as outer spectral peak is drastically enhanced. This results lead to a uncommon phenomenon that although lesser Re_τ value is achieved with blowing with higher amount of energy in the outer region of the boundary layer. According to such results, turbulent structures through out the boundary layer is assumed to be altered under the influence of uniform blowing. Therefore, such argument necessitates the present study which is however, intended to investigate the higher Reynolds number flow.

Stroh et al. (2016) investigated the effect of uniform blowing using DNS over a spatially developping TBL reaching a maximum of $Re_\theta = 2500$. This numerical study was conducted in terms of control and drag reduction perspective. Uniform blowing at an intensity of 0.5% U_∞ was applied from an upstream control region with a finite streamwise distance. They found that upstream blowing increases momentum thickness and simultaneously reduces drag which can be persistent far downstream from the control location. This was compared changing the control location and therefore, upstream control was found to be more effective than that of downstream placement. In other sense, integral drag reduction rate is higher when blowing is applied upstream near to the leading edge. 31% global drag reduction was achieved for the stated blowing intensity. However, information regarding high Reynolds number data or Reynolds number dependence at varying blowing ratio was also absent.

Marusic et al. (2014), studied the control of such organized motions applying rectangular jets in SBL flows, at $Re_{\tau,SBL} = 14000$. Using a single jet in order to control so called coherent structures (LSMs and VLSMs) was found to be feasible provided that jets are implemented in correct scale. Flow control using jets can be expensive in terms of energy consumption, therefore, difficult to implement in airplane surfaces. This leads to the present study using perforated surface designed in the order of δ.

5. High Reynolds number measurement

Large subsonic jet aircraft's are operated within chord Reynolds number range up to and beyond 10^7 (Lissaman (1983)). In order to improve the drag performance of aircraft surface, it is also necessary to evaluate the performance of the applied control technique in such a way that the performance parameters are comparable to the operating range. In contrast, experimental conditions are far beyond the operating range for control experiments in laboratory. Although, experiments provide important insight for the application but appropriate utilization of such results are still a matter of debate.

Canonical SBL flow is commonly known for its wide variation of scales. Multiple

studies during the last decade have convincingly proven that very large scale motions are present at all Reynolds numbers within a developed SBL. They have shown that their corresponding mean energy contribution and interaction with the near wall small structures increases along with the increasing Reynolds number (Smits et al. (2011)). Strong shear layer near the wall causes extreme fluctuation. As a result, turbulent production process is substantially modulated from the wall roughness. But as we go beyond a certain threshold of the Reynolds number where inner and outer region has sufficient separation in terms of their peak value, outer layer influence on the energy scale become comparable to the inner layer. With increasing Reynolds number beyond the threshold value, outer layer cycle reigns over the inner layer influence. HWA measurements at high Reynolds number facility from Hutchins and Marusic (2007a) indicate that shear Reynolds number of the experiment should be $\mathrm{Re}_\tau = 1700$ in order to observe at least one decade of separation in the streamwise fluctuation data. Where, most energetic peak location both in turbulence intensity and energy spectra is than under the scope of measurement to study. On the other hand uncertainty regarding inner peak location increases at high Reynolds number due to the probe effect for HWA measurements (Hutchins and Marusic (2009)). Therefore, studying the outer region using non-intrusive technique such as PIV offers comparatively less uncertainty and easy handling of large volume of measurement data.

Within the scope of present experiment, measurements from high Reynolds number SBL flow was obtained using PIV. Particularly, such data offers to investigate the contribution from the large scales in terms of production of the turbulence and hence, statistical manifestation of the control influence. This is to outline models which can efficiently control and reduce friction drag for aero-engineering applications operated at high Reynolds number regime.

6. Experimental procedure

In this section experimental facility used to obtain data will be discussed followed by the description of the measurement method itself.

In order to indicate different locations inside the wind tunnel, Cartesian co-ordinate system x, y and z direction is used to indicate streamwise (longitudinal), wall normal (vertical) and spanwise (transverse) direction respectively. In all cases streamwise direction on the surface of the present boundary layer was measured from the tripping location. Here, positive distance along x, y and z axis indicate further away from tripping, wall and wall centerline respectively. Reported boundary layer develops over the lower flat wall where an artificial tripping is installed exactly at the leading edge. Tripping is done with a 4 mm high spanwise metal bar followed by a grade 40 sand paper spacing $0.093m \times 2m$ in streamwise and spanwise direction respectively which facilitates direct transition to turbulent boundary layer. Therefore, with the help of tripping at the inlet, a thick boundary layer develops in the order of 0.24 m at a streamwise distance of $X = 19.2m$ from tripping.

Present experiment was conducted in zero pressure gradient condition e.g. difference between mean pressure gradient along streamwise direction was close to zero or Zero Pressure Gradient (ZPG) condition was assumed to ease the experimental condition. Moreover, this SBL condition also exhibit the analogous characteristics to different length scales of structures present to the application range. For this experiment, idealized environment was assumed using kinematic and geometric similarity. Stronger effort was directed towards the data acquisition in near wall region. Another particu-

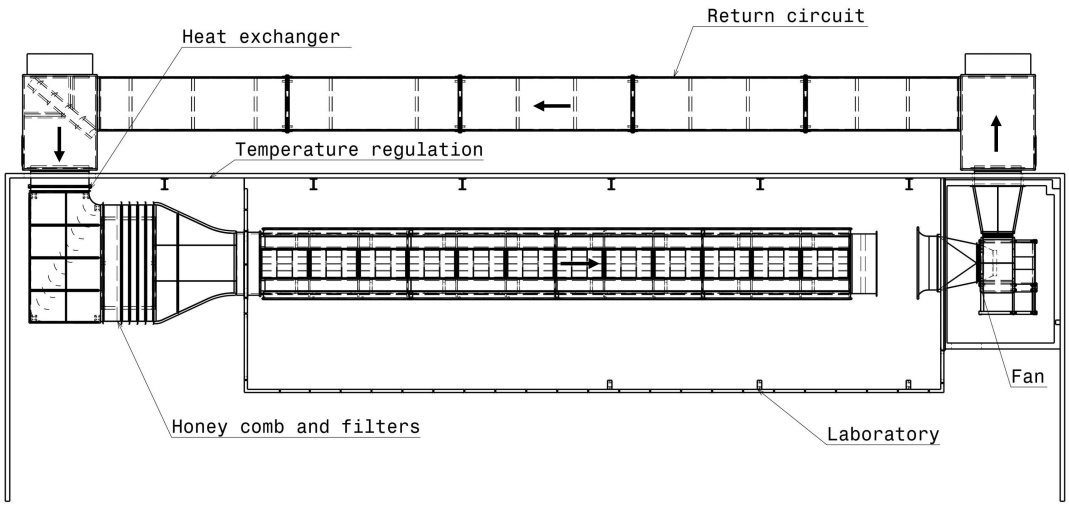

Figure 1.: Schematic of the top view of wind tunnel (Cuvier et al. (2017)). Primary flow path is indicated with arrows.

lar characteristics which is often neglected in such experiments is a steady outer flow required with low free stream turbulence level, which is in present case was lower than 0.25% than that of free stream values.

Only uniform blowing was applied in SBL cases as a mean to flow control. For reference SBL data boundary conditions at wall are as similar to the one as "no-slip" conditions e.g $[\bar{u}_x, \bar{u}_y, \bar{u}_z]_{wall} = (0, 0, 0)$ and at the outer edge of the boundary layer $[\bar{u}_x, \bar{u}_y, \bar{u}_z]_{\infty} = (U_{\infty}, 0, 0)$. Here, $\bar{u}_x$, $\bar{u}_y$ and $\bar{u}_z$ are the streamwise, wall normal and spanwise component of velocity averaged in time respectively and U_{∞} refers to the free stream velocity at the outer edge. Therefore, special consideration should be taken in order to interpret Reynolds number with subscript "SBL" as stated earlier. Such for uniform blowing measurements, boundary condition at the wall is, $[\bar{u}_x, \bar{u}_y, \bar{u}_z]_{wall} = (0, V_w, 0)$, here, V_w is the velocity of blowing applied in perpendicular direction coming from wall. Details of this blowing air parameter will be discussed in Section-6.2.

Within the scope of present literature, results are presented for $7495 \leq Re_{\theta,SBL} \leq 18094$, here, $Re_{\theta,SBL} = U_{\infty}\theta/\nu$ (with the momentum thickness (θ) and the free stream velocity (U_{∞})). The following flow condition is comparable to $2186 \leq Re_{\tau,SBL} \leq 5482$ using viscous parameter where $Re_{\tau,SBL} = \delta u_{\tau}/\nu$ which is also known as δ^+. Another important characteristics that is strongly influenced by the control technique is the shape factor ($H = \delta^*/\theta$) where δ^* is the displacement thickness. This parameter indicate not only the turbulent state of the boundary layer but also the modifications made to the mean properties when control is applied.

6.1. The wind tunnel facility

All measurements were carried out in the large boundary layer wind tunnel of "Laboratoire de Mécanique des Fluides de Lille – Kampé de Fériet (LMFL). This facility is particularly suitable for high resolution measurements at high Reynolds numbers of SBL. The wind tunnel used for this experiment has a closed loop configuration which is particularly suitable for non-intrusive optical measurements.

The test section of the wind tunnel is $20.6m$ long with a cross section of $2m^2$ with vertical and transverse lengths of 1 m and 2 m, respectively. As the test section has an optical access from all sides along the complete length of it, high quality PIV measurement through the optical access is possible. Figure-1 present the sketch of the wind tunnel drawn based on the top view of it. Incoming air to the plenum chamber is passing through an air-water heat ex-changer in order to provide an iso-thermal flow where efficiency is kept within $\pm 0.15°C$. Subsequently, air through the guide vanes undergoes a relaminarization process via honeycomb screens and grids. Thereafter, contraction takes place with a ratio of 5.4 : 1.

Free stream/external velocity (U_∞) can be regulated in the range of $3 \sim 9m/s$ at the entrance of the test section with a precision of $\pm 0.5\%$. The free stream turbulence is below 0.2 %. This wind tunnel allows us to investigate a wide range of local Reynolds number range based on local momentum thickness.

6.2. Uniform blowing setup and characterization

Uniform vertical blowing was provided with a perforated/blowing surface from the beginning of the test section at $x_1 = 18.424m$ and ends at a streamwise distance of $x_2 = 18.845m$. Figure-2(a) and Figure-2(b) displays the parallel and top view projection of the experimental segment of wind tunnel in 2D space respectively. In both cases, region of the wall from which uniform blowing was applied is indicated with pink region. Perforated surface is $0.55m$ and $0.42m$ in width and length respectively. This was placed symmetrically at spanwise center of the test section. Although, lower wall of the test section is composed of different segments, careful effort was provided to keep the streamwise alignment better than $0.1mm$.

Perforated surface is constructed from a $20mm$ thick stainless steel plate where 4514 holes were precisely drilled in staggered arrangement[3]. From Figure-2(c) exhibit the arrangement of the holes in top view to the wall frame of reference. Each holes were precisely drilled with a diameter of $3.6mm$, were organized from each other keeping their center $14.4mm$ in streamwise and $7.2mm$ in spanwise direction.

Perforated surface is comprised of different components attached together in order to form a box shaped device where air is remained sealed and can only be transmissible from inlet all the way through the perforated region. Therefore, the blowing device formed out of different sections and will be termed as "Blowing assembly" hereafter. Figure-2(d) displays isometric view of different segments where two additional surfaces between the air inlet and perforation was used along with other additional fixtures as such that the inlet air pressure is uniformly distributed inside the "Blowing assembly". Here, region marked with shaded pink indicate the opposite side of the perforated surface. Pneumatic sealing was used between each fixtures to prevent the air loss and was checked in every stage while assembling together. Blowing assembly was connected with four poly-amide air tubes equipped with Legris fast connectors through which dry compressed air was provided. Pressurized air was regulated with a pressure regulator and valve. The mass flow rate was measured with an appropriate vortex flow meter(accuracy $\pm 1.5\%$ on volume flow rate) and a temperature and pressure sensor to get the density (accuracy $\pm 1\%$). Total uncertainty on the imposed flow rate to get the desired velocity through the perforated wall is then $\pm 2\%$.

[3]Design of the holes arrangement was adopted from the Tailored Skin Single Duct (TSSD) design from Horn et al. (2015), this was discussed in detail from Krishnan and Bertram (2017). The original micro-perforated surface was designed for A340-300 with a hole diameter to to spanwise distance ratio of 1:2. Scale modification was done based on δ for spatially developped thick SBL condition such as LMFL wind tunnel.

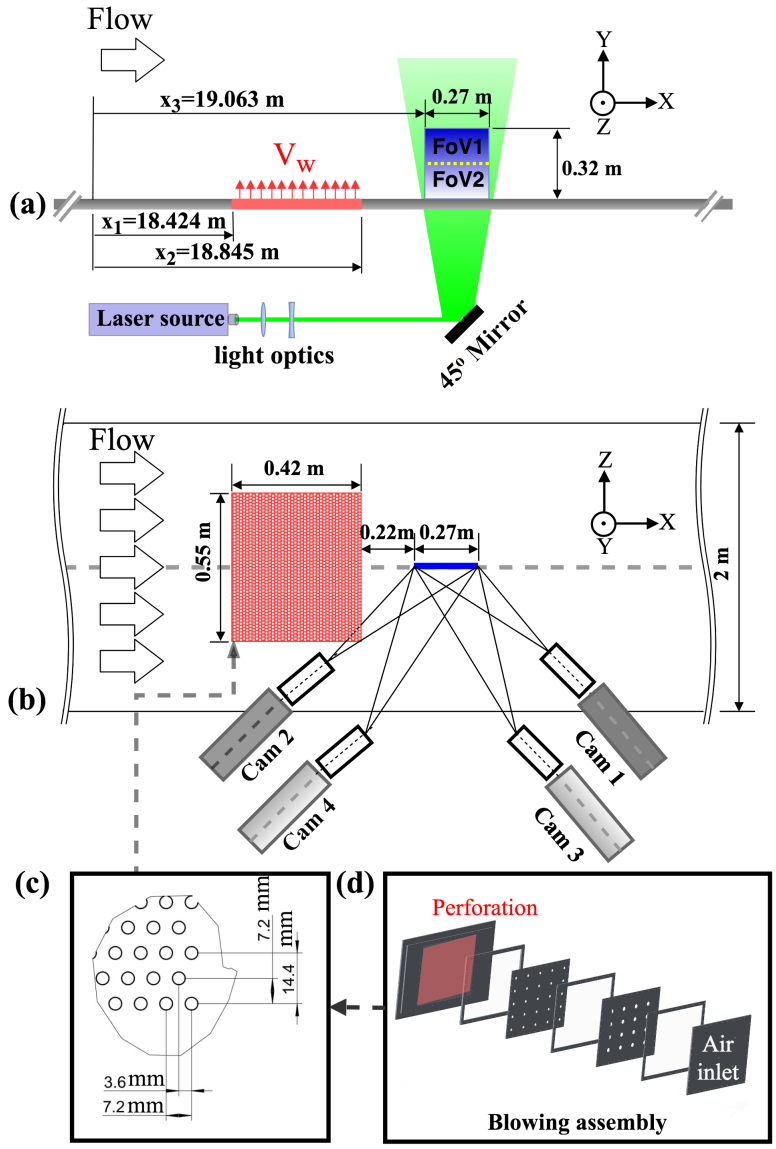

Figure 2.: (a) Parallel view scheme of uniform blowing experiment over flat plate SBL showing the laser light sheet and the measured field of view of the streamwise plane, location of uniform blowing is marked with the pink region, (b) Top view schematic of the same (c) Drawings showing the arrangement of holes and (d) Break down of different segments of blowing assembly

In order to quantify the magnitude of blowing, blowing fraction (F) will be used hereafter. This is simply the ratio in percentile between blowing velocity (V_w) and free stream velocity at the entrance of the test section. Therefore one can derive the formula for the blowing fraction as $F = (V_w/U_\infty) \times 100$. The blowing velocity ($V_w$) is determined by the total mass flux by the compressor and the sum of the perforated hole surfaces. For each Reynolds number being investigated, upstream blowing was varied in 4 different ratios, namely 0%, 1%, 3% and 6%. For each Reynolds number and blowing ratio, each data set will be termed as cases corresponding to the different

planes of measurement. Air flow rate for different blowing ratio was varied between $2 \sim 500m^3/hour$.

One of the primary objective of the present experiment was to investigate the effect of maximum blowing ratio which would be sustainable to keep the TBL profile before reaching into the potential layer (free stream). Maximum blowing ratio of 6% was selected as the maximum limit as it is already a strong mass flow rate injected compared to the one of the viscous sublayer (about 50 times at maximum velocity). The aim of the study is to find alternative flow control strategy so the energy injected should be as small as possible to get positive balance.

Measurements from a smooth surface SBL was also obtained in addition to the different ratios of blowing. Analysis of this data from upstream smooth wall will be used for wind tunnel characterization and to observe the changes in SBL mean properties compared to the different ratios of upstream blowing.

6.3. Particle image velocimetry (PIV)

In order to obtain all three components of the velocity, SPIV technique was used. The flow was successively measured in XY plane using SPIV arrangement. Description of this set-up will be discussed in the following section.

The velocity profiles downstream to the uniform blowing region acquired in a SPIV plane started after $0.22m$ from the end of the blowing region. Distance of this plane relative to the start of the test section is $19.063m$ downstream. The Field of View (FoV) as indicated with shaded blue in Figure-2(a) was $0.27m \times 0.32m$ in streamwise and wall normal direction respectively.

Laser light sheet was produced from a BMI laser with $200mJ/pulse$ through the bottom glass surface which is shown in Figure-2(a). Incoming laser beam was passing through a spherical ($f' = 5.6m$) lens placed at 0.5 m and a cylindrical ($f' = -0.25m$) lens placed at 0.75 m from the laser source outlet respectively before directed by a 45° mirror placed below the glass wall and 8.3 m downstream from the laser output (distance from beam exit to bottom glass is 9 m). Therefore, creating a light sheet with uniform thickness[4] of 0.6 mm as indicated with green in Figure-2(a). Two cavities of the pulsed laser were synchronized with the camera at a frequency $f_{acq} = 4$ Hz.

The SPIV set-up was consisting of 2 separate stereo systems placed on top of the other. Camera 1 and 2 (upper part of FoV), camera 3 and 4 (see Figure-2) will be termed as SPIV system 1 and 2 respectively for the subsequent discussion. Here, 4 sCMOS camera were used for this setup, each of the camera CMOS sensor array having streamwise and wall normal resolution of 2560×2160 pixel^2 with a pixel size of $6.5\mu m$. Larger pixels of each camera were aligned with the streamwise axis of the flow field i.e. larger side of the camera sensor was imaging streamwise extent of FoV. Each camera lenses were mounted with a $135mm$ Nikkor lens and was set at $f\# = 8$. The camera arrangement for XY plane is displayed in Figure-2(b), 2 cameras were arranged in angular configuration within each stereo system following the description from Prasad (2000). Complete FoV for XY plane was obtained with the overlapping of two planes acquired from each stereo system on top of the other where camera 1 and camera 2

[4]The laser sheet thickness was computed with laser beam propagation formula (non Gaussian beam with $M^2 = 1.2$). With the optic used, the half-angle divergence of a Gaussian laser beam (theta) was computed and the light sheet thickness which is then equal to the beam waist diameter $2 \times \text{lambda} \times M^2/(\pi \times \text{theta})$, with the laser wavelength, lambda = 532 nm. In order to confirm, the result was checked by making some light sheet impact on special paper, therefore, thickness of the light sheet was measured with binocular magnifier with an accuracy of ±0.1 mm.

was responsible for the top plane (FoV 1 in Figure-2(a)), Camera 3 and camera 4 was responsible for the bottom plane (FoV 2 in Figure-2(a)). Therefore, a common region was present between each field in the order of $10mm$ at y direction. In Figure-2(a), common region is indicated with the dotted yellow line. Cameras were mounted on a custom made bench with a Scheimpflug adapter, approximately $0.13m$ away from the test section glass wall (working distance of about 1.7 m). As summarized in the Table-1, magnification value was 0.083 in order to resolve most of the structures present in the logarithmic and outer region of the flow. With this value, the stretching factor of the stereo viewing angle (about 45deg) and the approximate value of the external velocity, a Δt was computed and impose to obtain about this 12 pixels displacement in the external region. Before recording, some random snapshots were taken and analysed rapidly in 2D2C to check that the correlation was working well with this 12 pixels dynamics. With these tests, we have optimised the Δt around the starting value to get high dynamic and good correlation (low number of spurious vector). The final Δt used was leading to 12 pixels displacement in the external region of the boundary layer with the 2D2C tests before recording (small correction compared to the first estimation).

Two cavities of the BMI laser was triggered with varying time delay of $\Delta t = 135 \sim 405\mu s$ depending on the Reynolds number of the flow. Acquisition frequency (f_{acq}) was set at a constant value of 4 Hz for each data set. A total of 3000 velocity fields were obtained with all three components of velocity where w (Z direction) component is the out of plane motion (Table-1).

The reconstruction was done according to the method proposed by Soloff et al. (1997) and a self-calibration similar to Wieneke (2005) was applied. The calibration was done by recording 21 pictures of a target at different z location (out-of-plane direction) from -5 to +5 mm with step of 0.5 mm. The analysis was done with MatPIV modified at LMFL with a multipass/multigrid approach (Willert and Gharib (1991), Soria et al. (1996)) with fours passes, starting with 64 by 64 then two of 32 by 32. The final Interrogation Window (IW) size was 18 x 24 (corresponding to 1.9 mm x 1.9 mm or about 45 wall-units at the highest Reynolds number). Before the final pass, image deformation was also used to improve the quality of the data (Scarano (2002)). The window overlap was set to 60 % in both direction. Final IW size determines the spatial resolution of the present measurement when expressed in wall units. Final IW varied between $15.3^+ \sim 43.2^+$ depending on the Reynolds number of the flow (see Table-1).

The flow was seeded with tracer particles by a Hazebase Base Classic fog machine located in the wind tunnel diffuser section. Particles are globally provided by a repeating evaporation and condensation process using a solution of poly-ethylene-glycol and water. The mean particle diameter is approximately 1 μm and have a lifetime of around 10 minutes circulated within the closed circuit wind tunnel.

A nomenclature stated in Table-1 indicate in a sequence the reference plane of measurement, free stream velocity, surface condition and rate of blowing fraction applied. Where, first 2 letters in capital 'XY' indicate reference plane of measurement from streamwise-wall normal plane, third letter 'U' followed by a fourth or fifth digit indicate free stream velocity and the fourth letter 'S' or 'F' indicate surface condition which is 'SBL' or blowing respectively. Finally, the last digit indicate the rate of blowing fraction applied. PIV images were processed using an in house (LMFL) modified version of MatPIV code. Image deformation due to stereoscopic aberration was adjusted using the Soloff back projection/re-construction of three dimensional warping technique (Soloff et al. , 1997). This is the same 3D warping technique described in Coudert and Schon (2001) and implemented in the calibration process described as "Self-calibration" applied in Wieneke (2005). Laser light sheet misalignment correc-

tion was done by cross-correlating the two PIV mapped images, which gives us the opportunity to correct the error on the 3D vector origin.

During calibration, a precision translation stage was used to offset along the corresponding calibration axis (z-axis). For the measurement in XY plane, the translation stage was moved in the spanwise direction for $-0.005m \leq z \leq 0.005m$ where each step was $\Delta z = 0.0005$. A sequence of 21 images for the calibration target were acquired on both stereo systems. Here, 0.8 m $\times$ 0.34 m rectangular calibration target was printed with dark crosses with a precision stretching of gap between each circles of 0.00916667 m and 0.0091591 m along x and y-axis respectively. Therefore, high degree of sharpness on the camera sensor was attained by applying optimal aperture ($f\# \geq 8$) of the mounted lenses and careful application of the Scheimpflug condition using the Scheimpflug adapters following Prasad and Jensen (1995).

A mesh of grid points were created in the physical space and were then projected into the camera space thanks to the Soloff function (Soloff et al. (1997)). The displacement is then evaluated on each camera on these projected grid which are not regular. Finally, Soloff reconstruction method was used to obtain the 3C velocity fields. Common grid points from the calibration target is then reconstructed using 2D2C component. Number of mesh points for top stereo system had a 334 points along x-axis and 206 points along y-axis with an increment of 0.0008 m along both the axis (corresponding to 7.435 pixel along x-axis or 9.682 pixel along y-axis). Therefore, recombination of both stereo systems provided a mesh steps of 334 and 402 in x-axis and y-axis respectively where, first mesh point along y-axis was determined at 0.0012 m or 14.5 pixels from the wall.

6.3.1. Measurement uncertainty

As discussed in sub-section-6.3, SPIV system-1 and system-2 had grid points (measurement point in the object plane) [$N_{x,sys1}$, $N_{y,sys1}$], [$N_{x,sys2}$, $N_{y,sys2}$]=[334 , 206], [334, 206]. Merging of the two overlapping system took place at the intersection of the both systems and causes an overlapping of 334 and 10 vector points in streamwise and wall normal direction .

Plane (1-2)		XY	
Stereoscopic angle		45°	
Focal Length (mm)		135	
Laser sheet thickness (mm)		0.6	
Magnification		0.083	
Lens aperture ($f\#$)		8	
Lens working distance from FoV (m)		1.7	
FoV (m × m)		0.27 × 0.32	
CMOS array [x × y] (px × px)		2560 × 2160	
Overlap region in 'y' (mm)		10	
Image acquisition frequency (Hz)		4	
IW size [mm × mm]		1.9 × 1.9	
No. of records		$3{\times}10^3$	
SBL Reynolds number ($Re_{\theta,SBL}$)	7500	12500	18100
IW size [L_{IW}]($y^+ \times y^+$)	15.3×15.3	29.7×29.7	43.2×43.2
FoV [$S_{x,1}$,$S_{y,1}$]	1δ, 1.2δ	1.1δ, 1.32δ	1.1δ,1.33δ
Mesh step [Δ_i/l^+_{SBL}] (y^+)	6.5^+	12.5^+	18.5^+
Integral time scale [Λ] (s)	0.081	0.036	0.024
Convergence uncertainty on $\bar{u}$,			
- SBL [$U_{\bar{u},SBL}$](%)	±1.1	±0.7	±0.7
- at F=0% [$U_{\bar{u},F0}$](%)	±1.1	±0.8	±0.7
- at F=1% [$U_{\bar{u},F1}$](%)	±1.2	±0.8	±0.7
- at F=3% [$U_{\bar{u},F3}$](%)	±1.2	±0.9	±0.8
- at F=6% [$U_{\bar{u},F6}$](%)	±1.4	±1.1	±1.1
Convergence uncertainty on $\sqrt{\bar{u'^2}}$, [$U_{u_{rms}}$](%)		5.1	
Rec.			
- SBL	`XYU3S`	`XYU6S`	`XYU10S`
- at F=0%	`XYU3F0`	`XYU6F0`	`XYU10F0`
- at F=1%	`XYU3F1`	`XYU6F1`	`XYU10F1`
- at F=3%	`XYU3F3`	`XYU6F3`	`XYU10F3`
- at F=6%	`XYU3F6`	`XYU6F6`	`XYU10F6`

Table 1.: PIV recording parameters

Thus merging region extends in 10 and 333 points along wall normal and streamwise directions respectively, e.g. number of grid points along X and Y axis for the merging region would be [$N_{x,m}$, $N_{y,m}$] = [333, 10]. Merging of two separate Stereo systems is done by simply taking the average of each component from two 2D3D velocity fields. Therefore, SPIV bias error and random PIV uncertainty can be estimated following the procedure proposed by Kostas et al. (2005), Herpin et al. (2008) and Cuvier (2012).

Total uncertainty on the mean velocity components of a 2D3C field can be calculated using the velocity data for two separate SPIV systems within the merging region. Equation-1 is used to determine the bias error or the PIV uncertainty. Here, u_{sys1} and u_{sys2} represent the streamwise velocity component for SPIV system 1 and 2 respectively. Similarly, bias error for wall normal (v) and spanwise (w) component of the velocity field was obtained using difference between simultaneous image pairs of two systems in the merging region.

The random PIV uncertainty (σ_{ϵ_u}) with 95% confidence interval for the streamwise

$Re_{\theta,SBL}$	Rec.	Bias error (%U_∞)			Random error (%U_∞)		
		-u	-v	-w	u	v	w
7500	XYU3S	0.03	0.03	0.07	0.6	0.5	0.8
12500	XYU6S	0.04	0.03	0.06	0.7	0.6	0.9
18100	XYU9S	0.03	0.04	0.06	0.9	0.5	1.1

Table 2.: SPIV error analysis using the overlapping region. The errors are given in percentage of U_∞.

velocity component is determined using Equation-2. This equation is also applicable in determining the random error for wall normal (σ_{ϵ_v}) and spanwise (σ_{ϵ_w}) component of the velocity. Table-2 compiles the error estimated at streamwise and wall normal distances of [X/δ, Y/δ, $Re_{\theta,SBL}$] = [70.41,0.58, 7495], [78.46, 0.64, 12542] and [79.14, 0.65, 18094]. Here, bias and merging error for all three component is compiled as a fraction of U_∞. In table-2, $Re_{\theta,SBL}$ and Rec. indicate the reference SBL case and corresponding labelling respectively similar to the Table-1.

$$\Delta u = \pm\langle u_{sys1} - u_{sys2}\rangle \tag{1}$$

$$\sigma_{\epsilon_u} = \pm(u_{sys1} - u_{sys2})_{RMS} \tag{2}$$

6.3.2. Convergence of data

PIV images were acquired as such that statistically independent measurement at 4 Hz were taken for each recordings. Although, there remains a question regarding statistical convergence of the data. It is therefore, important to obtain sufficient amount of ensembles in order to have acceptable convergence. For turbulent flows such as TBL, large gradient of the mean streamwise velocity is present from the region of high frequency fluctuations to the regions with lower frequency fluctuations. Kähler et al. (2016), has showed the convergence of moments from the streamwise fluctuation for different sampling rate. They showed that, data points in the free stream region converges faster than the near wall regions. In addition, they recommend that atleast 1000 samples through time are required to obtain the first and second order statistics correctly. Therefore, it necessitates a convergence study for the data presented here.

Dixon and Massey (1957) suggested that statistical convergence uncertainty on a sample mean and standard deviation with 95% confidence interval (and Gaussian distribution) can be calculated using Equation-3 and Equation-4 respectively. Here, both equations are derived for the streamwise velocity component. Similar expressions can also be derived for wall-normal and spanwise velocity component. N_{eff} is the total

U_∞ (m/s)	u_τ (m/s)	ν/u_τ (μ/s)	C_f [$\times 10^3$]	δ (m)	δ^* (m)	θ (m)	H -	Re_x [$\times 10^6$]	Re_θ [$\times 10^3$]	Re_{δ^*} [$\times 10^3$]	Re_τ -
3.4	0.121	124	2.53	0.271	0.045	0.0331	1.36	4.33	7.5	10.2	2186
6.78	0.2345	64	2.4	0.243	0.037	0.0277	1.32	8.64	12.5	16.5	3800
10.14	0.3455	44	2.32	0.241	0.0348	0.027	1.3	12.93	18.1	23.5	5482

Table 3.: Mean properties (for reference cases) of the SBL in LMFL wind tunnel at X = 19.2 m obtained from SPIV measurement: U_∞, free stream velocity; $u_\tau \equiv \sqrt{\tau_w/\rho}$, friction velocity; ν/u_τ, viscous length scale; $C_f = 2(u_\tau/U_\infty)^2$, friction coefficient; δ at $\bar{u}$ =99% U_∞; $\delta^* = (\sum_{y=0}^{\infty}(1 - \bar{u}/U_\infty))$, displacement thickness; $\theta = \sum_{y=0}^{\infty}(\bar{u}/U_\infty)(1 - \bar{u}/U_\infty)dy$, momentum thickness; $H = \delta^*/\theta$, shape factor; $Re_x = U_\infty X/\nu$, Reynolds number based on characteristics length; $Re_\theta = U_\infty\theta/\nu$, Reynolds number based on local momentum thickness; $Re_{\delta^*} = \delta^* U_\infty/\nu$, Reynolds number based on local displacement thickness; $Re_\tau = \delta u_\tau/\nu$, Reynolds number based on local friction velocity.

number of time steps or total number of samples acquired with statistical independence. In addition, Ahn and Fessler (2003) suggested that error rate for the following formulae are less than 1% when no of samples$\geq$ 30. In order to confirm that the samples were uncorrelated in time, time separation between two samples were selected as such that the sampling rate was less than 1/2$\times$integral time scale as suggested by Benedict and Gould (1996), provided that the total acquisition time was fixed. Here, integral time scale was calculated with $\Lambda = \delta/U_\infty$. In other words, sampling rate was 3 to 10 times larger than that of the integral time scale depending on the Reynolds numbers. In the present experiment, total number of samples acquired e.g N_{eff}=3000 at acquisition frequency of 4 Hz which corresponds to sampling rate more than 2Λ. Convergence uncertainties on the mean and turbulence intensity from streamwise velocity component is therefore, presented in Table-1.

$$U_{\bar{u}} = \frac{\Delta\bar{u}}{\bar{u}} = \pm\frac{1.96}{\sqrt{N_{eff}}} \times \frac{\sqrt{\bar{u'^2}}}{\bar{u}} \tag{3}$$

$$U_{u_{rms}} = \frac{\Delta\sqrt{\bar{u'^2}}}{\sqrt{\bar{u'^2}}} = \pm 1.96\sqrt{\frac{2}{N_{eff}}} \tag{4}$$

6.4. Boundary Layer Characterization

A priori to the control application using uniform blowing, experimental facility was characterized using conventional smooth surface. Characterization was done using the similar SPIV setup described earlier except wall shear determination. Recently, Willert (2015) conducted high magnification PIV experiments in the same facility

where very accurate determination of wall shear was possible. In the present experiment, wall shear was obtained using the same method for the recording`XYU3S`, `XYU6S` and `XYU10S`(Foucaut et al. (2018)). These data sets represent the characterization parameters for *SBL* condition with smooth surfaces. Table-3 summarized the mean properties of the SBL reference cases. Later mean properties with the application of MBT is also determined using the same streamwise stereo PIV set-up, except wall shear which was not determined. No additional suffix was used for the reference cases as normalization to these cases are done using respective inner and outer parameters.

6.5. Validation

6.6. SBL mean properties

As the size of the field of view is only of the order of one boundary layer thickness, the streamwise direction can be taken as homogeneous direction following an approach law $\delta/x = 0.37Re_x^{-0.2}$ from Schlichting (1979). Therefore, data presented for mean statistics is then averaged in both time and space as the FoV in streamwise direction was less than the boundary layer thickness in streamwise direction.

Mean streamwise velocity and corresponding wall normal distance is expressed as U^+ and y^+ in Equation-6. Literature suggestion regarding the extent of these layers are, viscous sub-layer: $0 \leq y^+ \leq 3-5$, buffer layer: $3-5 \leq y^+ \leq 30$ and log layer: $30 \leq y^+ \leq 0.1\delta^+$. Although, there are several arguments regarding the exact determination of these layers, but this paper only deals with the effect of blowing.

$$P = -\overline{u'v'}(\frac{\partial U^+}{\partial y^+}) \tag{5}$$

$$U^+ = \frac{1}{\kappa}\ln(y^+) + C \quad \text{for } 30 \leq y^+ \leq 0.1\delta^+ \tag{6}$$

where,

$$U^+ = \overline{u}/u_\tau$$
$$y^+ = yu_\tau/\nu$$

In order to show the quality of the XY stereo PIV plane to extract mean and turbulent profiles, first, in Figure-3, mean streamwise velocity profiles of SBL cases are drawn along with Van Driest profile following Equation-7 (Van Driest (1956)) and logarithmic profile following Equation-6. Inset figure is given in order to enlarge the near wall region and a good merging of the experimental data to the Van Driest profile can be observed. In Equation-7, $A^+ = 26$, The value of Von Karman constant (κ) and C is taken as 0.40 and 5.3 respectively. First data for $Re_{\theta,SBL} = 7495$, 12542 and 18095 were obtained at $y^+ = 16$, 31 and 45 respectively. At sufficient spatial resolution, SBL profiles at all three Re displays distinct logarithmic and wake region. In general, logarithmic region starts at $y^+ \approx 30$ and ends at ≈ 400, 700 and 1000 from lowest to highest Re. Boundary layer characteristics of SBL cases are reported in Table-1. Interested readers are advised Foucaut et al. (2018) for details of the measurement technique.

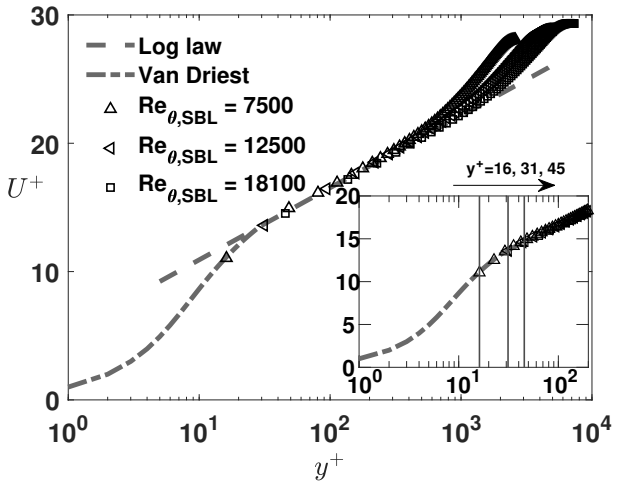

Figure 3.: SPIV data from XY plane for reference *SBL* cases. Mean streamwise velocity in wall units (U^+) plotted against dimensionless wall units (y^+). In the inset figure, same data is plotted in order to highlight the merging of the experimental data to the Van Driest profile within near wall region. One out of every five data point are presented for clarity.

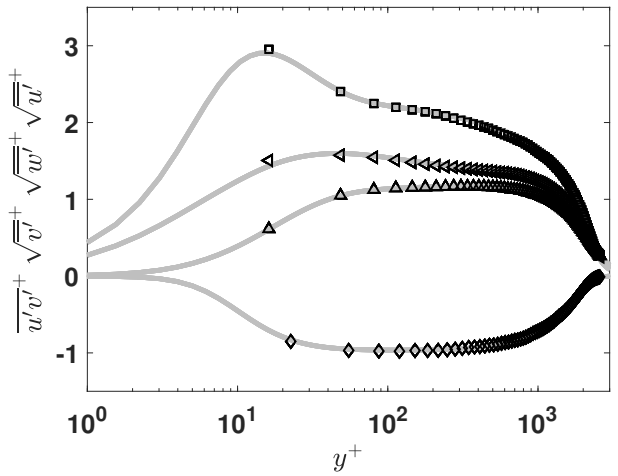

Figure 4.: Profiles of RMS values (turbulence intensities) of velocity fluctuations and RSS obtained. SPIV data (markers) is compared with LES data (continuous line). ——, LES data at $\mathrm{Re}_\theta = 7603$ from Eitel-Amor (2014) and markers represent present SPIV data at $\mathrm{Re}_\theta = 7495$: □, $\sqrt{\overline{u'^2}}/u_\tau$;△, $\sqrt{\overline{v'^2}}/u_\tau$; ◁, $\sqrt{\overline{w'^2}}/u_\tau$ and ⋄, $\overline{u'v'}/u_\tau^2$.

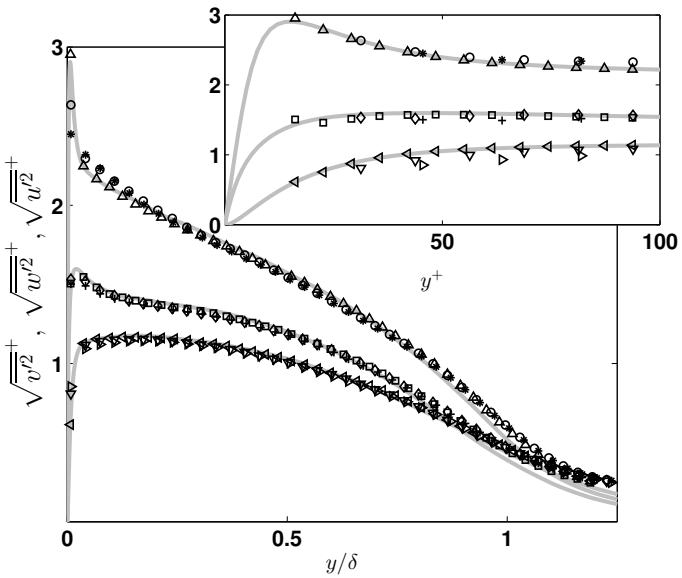

Figure 5.: Profiles of turbulence intensities: ——, LES data at $\mathrm{Re}_\theta = 7603$ from Eitel-Amor (2014) and symbols represent the present SPIV data in XY plane; $\sqrt{\overline{u'}}^+$, $\sqrt{\overline{v'}}^+$ and $\sqrt{\overline{w'}}^+$ are presented for all SBL cases respectively with: $\triangle$, $\triangleleft$, and $\square$, at $\mathrm{Re}_{\theta,SBL}$ = 7500; $\circ$, $\triangledown$ and $\diamond$ at $\mathrm{Re}_{\theta,SBL} = 12500$; $*$, $\triangleright$ and $+$ at $\mathrm{Re}_{\theta,SBL} = 18100$.

$$U^+(y^+) = \int_0^{y^+} \frac{2dy^+}{1+\sqrt{1+4\kappa^2 y^{+2}[1-exp(-y^+/A^+)]}^2} \quad \text{for} 0 \leq y^+ \leq 55 \qquad (7)$$

Then Figure-4 shows the turbulence intensity of u, v and w components scaled with the inner parameters and compared to the finely resolved LES data at $\mathrm{Re}_{\theta,SBL} = 7603$ from Eitel-Amor (2014). In order to obtain clarity for the experimental data in the figure, one out of every five data points are plotted here. Both LES and experimental data shows excellent agreement except the first data from experiment. Reflection from the wall is very common problem observed for PIV experiments.

Figure-5 shows the profiles of turbulence intensities for all three components obtained for all SBL cases (at $\mathrm{Re}_{\theta,SBL} = 7500$, 12500 and 18100). Here, markers represent experimental data obtained with SPIV measurements and continuous line represents the LES data from Eitel-Amor (2014). One out of every ten data is plotted in the following figure in order to have better clarity except the enlarged figure. Turbulence intensity profiles for three Reynolds numbers are scaled in wall units and as a function of both y/δ and away from the wall. Inset figure is plotted for the same data as a function of y^+ in order to enlarge the near wall region. Very good universality is observed for both representations along with the numerical data. Although a certain deduction regarding near wall peak value is not possible due to lack of data from SPIV which is solved in the paper of Foucaut et al. (2018) by combining the result with high magnification PIV.

Figure-6 shows the profiles of RSS normalized with inner velocity ($\overline{u'v'}/u_\tau^2$). This is obtained for the same data and compared to the same LES data as stated before. Zagarola and Smits (1998) suggested that the outer scaled wall location to the inner

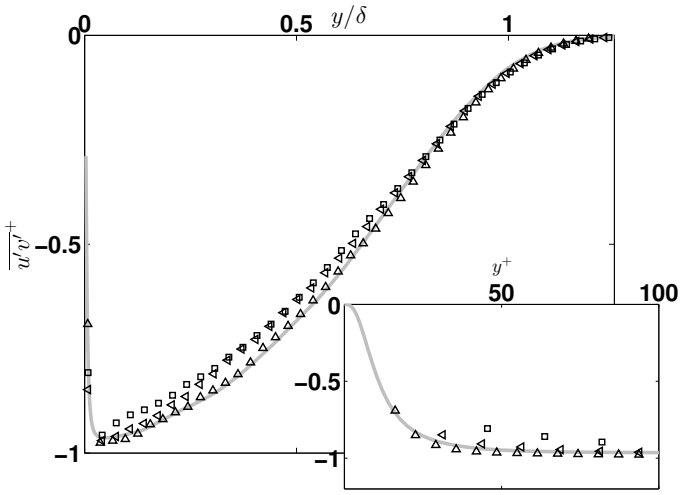

Figure 6.: Profiles of RSS ($\overline{u'v'}^+$): ——, LES data at $\mathrm{Re}_\theta = 7603$ from Eitel-Amor (2014) and symbols represent the present SPIV data in XY plane; △, $\mathrm{Re}_{\theta,SBL} = 7500$; ◁, $\mathrm{Re}_{\theta,SBL} = 12500$ and □, $\mathrm{Re}_{\theta,SBL} = 18100$;

scaled RSS exhibit a better Reynolds number independence atleast in the outer region, therefore, wall locations are normalized with the corresponding outer length scale e.g δ. In addition, inner scaled representation of the data is presented for the region $0 \leq y^+ \leq 100$. Although Reynolds stresses are being sensitive parameter when compared in a wide range of Reynolds number measurements. A slight variation in the near wall region can also be related to the increasing filtering with Reynolds number. But numerical data agrees well to the corresponding nearest data set ($\mathrm{Re}_{\theta,SBL} = 7495$). In particular, near wall presentation as a function of y^+ exhibit better universality than the y/δ presentation.

Figure-7 (a) plots the turbulence production (Equation-5) along inner scaled wall normal locations in logarithmic abscissa. LES data from Eitel-Amor (2014) is compared with all SBL data at three Re investigated. All data in the plot collapse well to each other. This inner scale scaling of the production confirmed that it is a near wall effect. Here, Figure-7 (b) is presented in pre-multiplied suggested by Marusic et al. (2010a) along their corresponding dimensionless wall locations in order to represent the equal areas which shows equal contributions to the bulk production term. For each Reynolds number investigated, all production profiles display a clear peak in the outer region and agrees well to the numerical data for the lowest Reynolds number.

Vallikivi et al. (2015a) showed from measurements at high Reynolds number that the skewness profiles of SBL is well collapsed using inner coordinates over the region of $100 < y^+ < 0.15Re_\tau$. They have also showed that skewness values are approaching negative values at $\mathrm{y}^+ \approx 200$ before finally reach a value of $S \approx -0.1$. Finally, skewness values are more negative in the wake due to intermittency, where they collapse well with the outer coordinates.

Figure-8 (a) and (b) shows the skewness $S(u) = < u^3 > / < u^2 >^{3/2}$ profiles of streamwise velocity plotted with inner and outer scales respectively for SBL cases. Although Figure-8(a) exhibit Reynolds number dependence for the outer region when scaled with inner length scales but a fairly good collapse of the same region can be seen in Figure-8(b) for all Reynolds number when scaled with the outer length scale. In all cases skewness is slightly positive near the wall for $\mathrm{y}^+ < 200$ and gradually

becoming more negative as the distance from the wall increases. In order to compare the accuracy, LES results at $\mathrm{Re}_\theta = 7603$ from Eitel-Amor (2014) are also plotted as gray continuous line. Present SPIV data agrees well to the similar description of the skewness profiles from Vallikivi et al. (2015a).

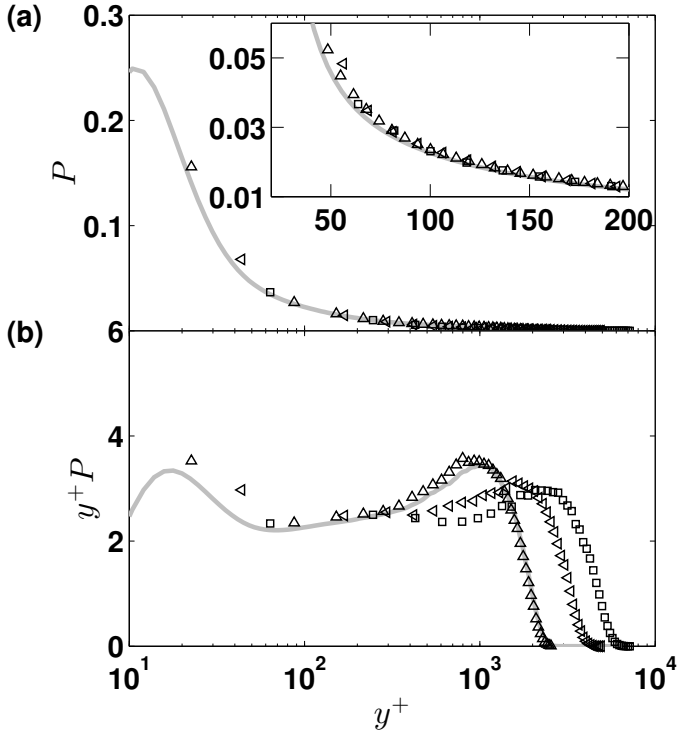

Figure 7.: Profiles of turbulent production (Equation-5): ——, LES data at $\mathrm{Re}_\theta = 7603$ from Eitel-Amor (2014) and symbols represent the present SPIV data in XY plane; △, $\mathrm{Re}_{\theta,SBL} = 7500$; ◁, $\mathrm{Re}_{\theta,SBL} = 12500$ and □, $\mathrm{Re}_{\theta,SBL} = 18100$; For clarity, one out of every ten data is presented.

The kurtosis $< u^4 > / < u^2 >^2$ profiles for the same data is shown in Figure-8(c) with inner scaling and (d) with outer scaling respectively. Inner coordinates shows Reynolds number dependence in the outer region but good convergence is obtained when plotted using outer coordinate. In both cases comparison to the numerical data has an excellent agreement.

Figure-9 shows the power spectra of u' from present SPIV measurement for $\mathrm{Re}_\theta = 18094$. Detailed spectral analysis can be found from Foucaut et al. (2004). In order to examine the k_x^{-1} dependence, wall scaled (Vallikivi et al. (2015b)) spectral energy of streamwise fluctuation Φ_{uu} is plotted against wall scaled spatial wave number (k_x) in typical log-log form for $0.045 < y/\delta < 0.1$. A common overlapping region or plateau is observed following -1 slope with fairly good collapse. However, due to the difficulties of converging the spectrum, this -1 slope can not be confirmed as Srinath et al. (2018) suggested that the slope is slightly different from -1 which varies from wall distance. This common region covers almost a decade in the wave number space. Present data is limited to the FoV size and large scales are larger than that of FoV, therefore, large scale energy spectrum was not covered from the present measurements.

7. Micro-blowing results and discussion

In this section, the changes in boundary layer caused by blowing is introduced. Blowing significantly increases the momentum thickness and the relationship is linear. Although uniform blowing is known for its boundary layer thickening properties, present SPIV data shows that boundary layer growth rate is even stronger at higher Reynolds number.

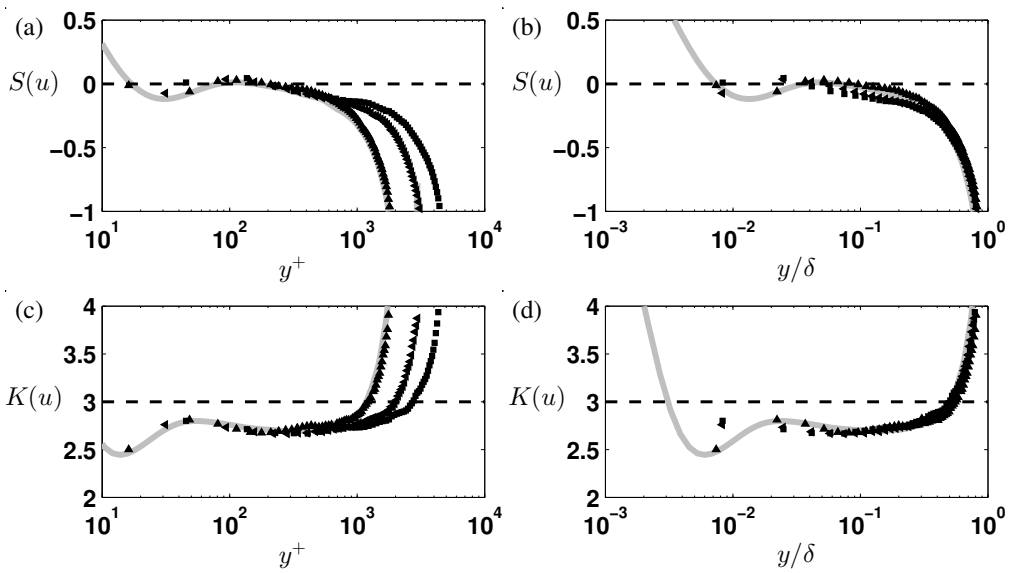

Figure 8.: Skewness and Kurtosis profiles along wall normal direction for SBL cases. ——, LES data at $\mathrm{Re}_\theta = 7603$, Filled symbols represent the SPIV data as the same notation used in Figure-6. Note that only one out of every five data along wall normal distance is presented for clarity. (a) and (c); inner scaled, (b) and (d); outer one.

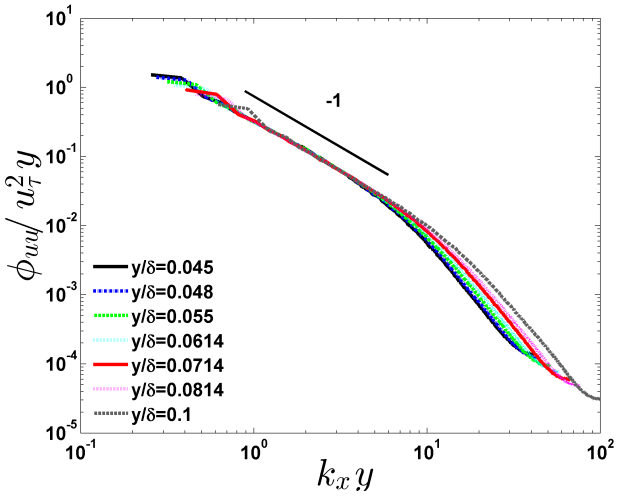

Figure 9.: Wall scaled power spectra of u' at different wall normal location obtained from SPIV data at XY plane for $\mathrm{Re}_\theta = 18094$. The solid black line indicates the k_x^{-1} dependence as guide for the eye.

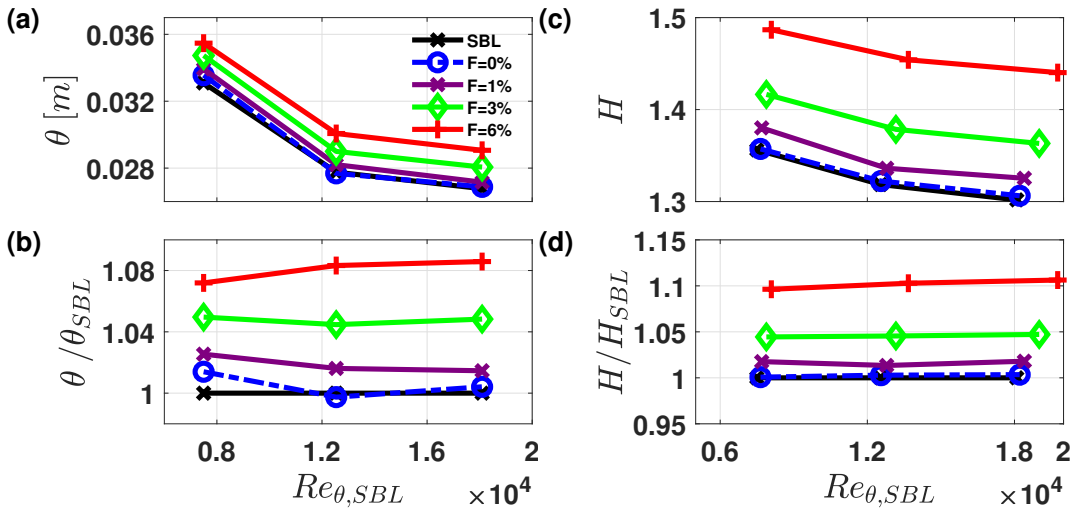

Figure 10.: Variations of momentum thickness (θ) and shape factor (H) in comparison to the $\mathrm{Re}_{\theta,SBL}$ for all cases investigated, (a) Momentum thickness (b) Growth of momentum thickness, (c) Shape factor and (d) growth of shape factor in comparison to the SBL cases.

Figure-10 (a) indicates the increase of momentum thickness with blowing ratio (F). Change of momentum loss is also presented in Figure-10 (b). Along all the Reynolds number investigated, rate of increase of momentum is almost uniform at a fixed blowing ratio. This indicates that the blowing ratio (F) can be used as an identity parameter in order to compare with the SBL cases as identified by Kametani and Fukagata (2011).

Similarly, Figure-10 (c) and (d) present the shape factor (H) and rate of change with blowing ratio for each case investigated. The shape factor increases with blowing ratios for all cases. As for the momentum thickness, the shape factor increases with blowing rate with same ratio compared to reference case for all Reynolds number

investigated (see Figure-10d). Combining the observations on θ and H, the increase of blowing ratio determined the increase of boundary layer thickness (δ) independently of the Reynolds number studied. The difference between rate of change of shape factor for SBL and perforated surface without blowing is negligible as inside the uncertainty level. Therefore, it can be inferred that effect of roughness from perforated surface is also negligible at least for the range of Reynolds number measured in the present paper. Kametani and Fukagata (2011) and Kametani et al. (2015) also suggested that blowing increases the boundary layer thickness, momentum thickness and the shape factor. Although, present measurement agrees to the DNS result trend of the mentioned papers, DNS overestimate the growth rate of the stated mean properties. There are two possibilities of such deviation: firstly, growth rate of mean properties reduces with increased blowing or secondly, blowing effect is more prominent at low Reynolds number. The second hypothesis can be privileged as the growth rate of θ and H with blowing ratio F is nearly linear and independent of momentum Reynolds number.

Mean streamwise velocity profiles are plotted in Figure-11 for the different blowing ratio and momentum Reynolds number studied. As stated earlier in Subsection-6.4, wall locations are normalized with the SBL cases which enables the present data to be compared without the biased effect of friction velocity (for the present experiment, friction velocity for the blowing cases were not determined). Most often, measurements of wall shear stress and shear velocity is difficult at high Reynolds number, therefore present scaling helps to ease the process of obtaining the scaling parameters accurately.

Streamwise velocity data is averaged over time and space before plotted as velocity profiles in Figure-11 (a), (b) and (c) at $\mathrm{Re}_{\theta,SBL} = 7500$, 12500 and 18100 respectively. Experimental data from Kornilov (2012), DNS and well resolved LES data from Kametani and Fukagata (2011) and Kametani et al. (2015) respectively have already showed that mean streamwise profile is pushed away from the wall and the effect of blowing is distinct in the outer layer, in particular numerical data exhibit these profiles more prominently where complete profile is influenced eventually. Contrary to the later part of this deduction, present data exhibit that only the inner layer is pushed away from the wall before merging in the wake. This is valid for all blowing ratios at all Reynolds number. Wall roughness effect of the perforated plate without blowing is also found negligible when compared to the SBL cases. This can probably be linked to the large difference in Reynolds number in the present study.

In addition to the mean streamwise profiles, RMS of turbulence fluctuations for all velocity components are presented in Figure-12 using inner scales from SBL cases. Here, Figure-12 (a), (d) and (g) presents RMS of streamwise velocity fluctuation, (b), (e) and (h) wall normal and (c), (f) and (i) presents spanwise fluctuation respectively. Therefore, turbulence intensities for all three components are enhanced in the outer region with a clear peak between 200+ to 500+ which grows with blowing ratio. A similar peak appears near this position for high Reynolds number boundary layer links with large scale structures (Hutchins and Marusic (2007b)). It can then be hypothesized that the blowing enhance the large scale structures. Then the effect of blowing diminishes at the beginning of wake region. Present measurement indicates a very interesting phenomena that the near wall region is almost unaffected through blowing while the outer and logarithmic part is strongly altered upto about 1000+.

Turbulence kinetic energy ($k^{+,SBL}$) is plotted in Figure-13 calculated using Equation-8 after normalized with the inner variables obtained from SBL cases. Here, different blowing ratios are indicated with colors as used in Figure-10(a).

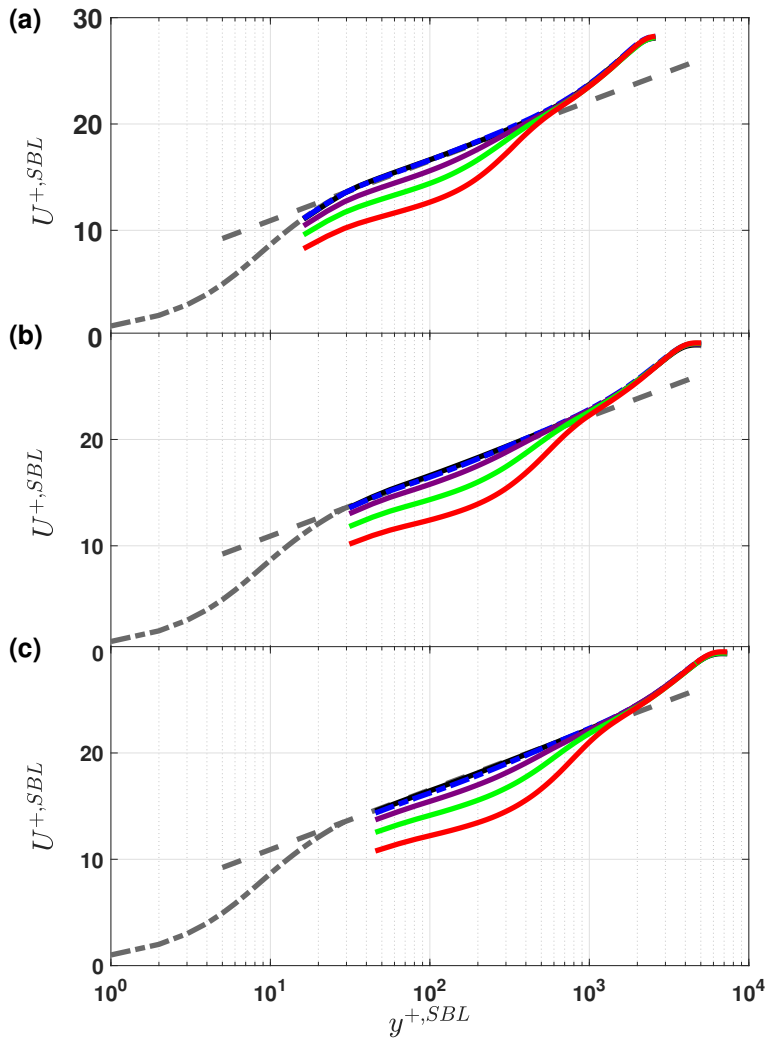

Figure 11.: Mean streamwise velocity profiles for different blowing ratios and momentum Reynolds number studied. In all cases inner variables from the reference SBL cases are used for normalization. Different blowing ratios are indicated with colors as used in Figure-10(a). Different Reynolds numbers are depicted in: (a) $\mathrm{Re}_{\theta,SBL} = 7500$, (b) $\mathrm{Re}_{\theta,SBL} = 12500$ and (c) $\mathrm{Re}_{\theta,SBL} = 18100$, Van Driest profile is plotted using 'dashed-dotted' line following Equation-7 and logarithmic profile is plotted using 'dashed' line following Equation-6 respectively.

$$k^{+,SBL} = 0.5\frac{\sqrt{\left((\sqrt{\overline{u'^2}})^2 + (\sqrt{\overline{v'^2}})^2 + (\sqrt{\overline{w'^2}})^2\right)}}{u_\tau} \tag{8}$$

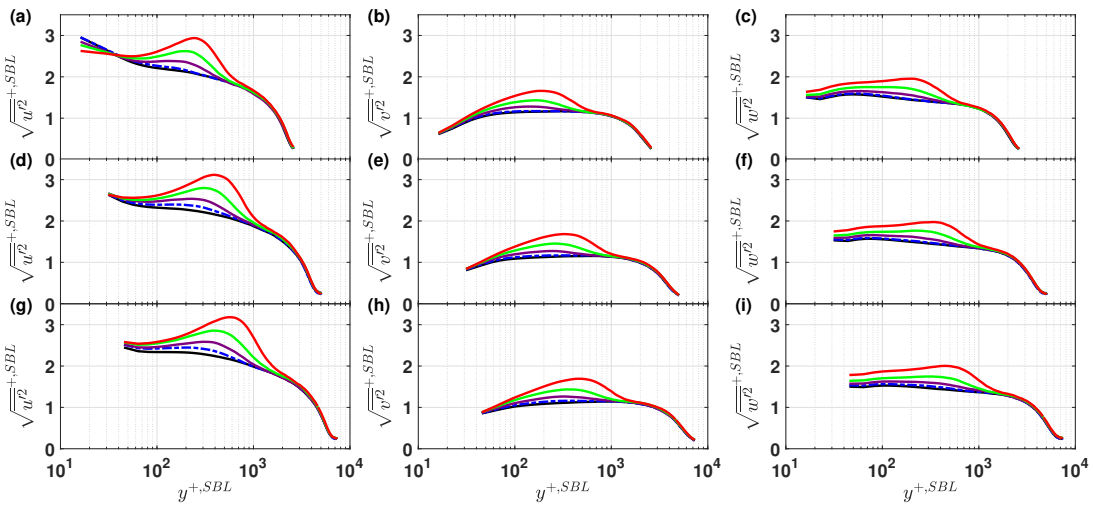

Figure 12.: Root-mean-square of turbulent fluctuations in streamwise, wall-normal and spanwise components. While different blowing ratios are indicated with different colors as used in Figure-10(a). (a), (b) and (c) for $\mathrm{Re}_{\theta,SBL} = 7500$; (d), (e) and (f) for $\mathrm{Re}_{\theta,SBL} = 12500$; (g), (h) and (i) for $\mathrm{Re}_{\theta,SBL} = 18100$.

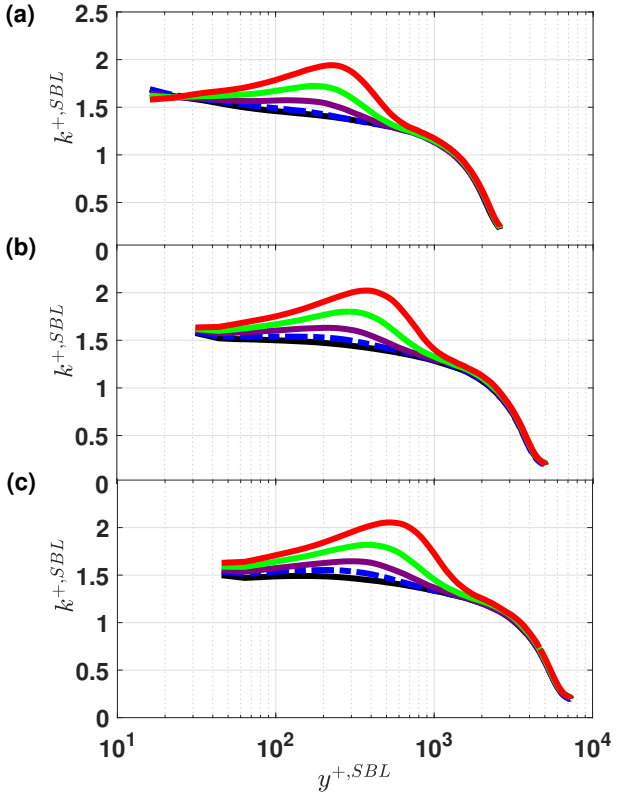

Figure 13.: Logarithmic profiles of $k^{+,SBL}$ along different wall normal locations ($y^{+.,SBL}$). Different Reynolds numbers are depicted in: (a) $\mathrm{Re}_{\theta,SBL} = 7500$, (b) $\mathrm{Re}_{\theta,SBL} = 12500$ and (c) $\mathrm{Re}_{\theta,SBL} = 18100$.

Subsequently, Figure-14 (a) plots the positions of outer streamwise component peak

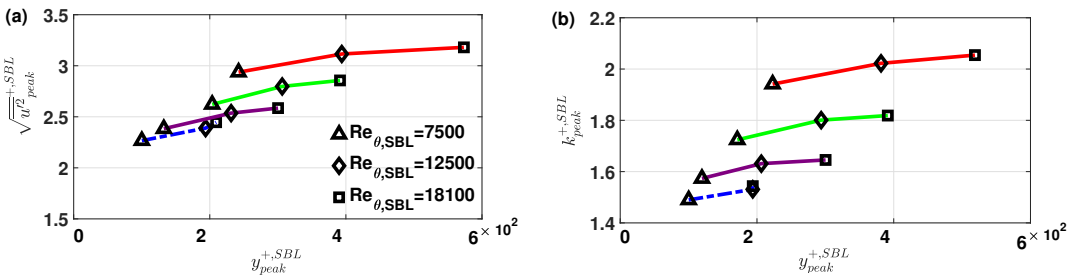

Figure 14.: (a) Outer peak values of $\sqrt{\overline{u'^2}}^{+,SBL}_{peak}$ and their corresponding wall normal position $y^{+,SBL}$ normalized with inner variables obtained from reference SBL cases. Different colors indicate blowing ratio as stated in Figure-10 (a). Symbols indicate reference $Re_{\theta,SBL}$, (b) Peak of $k^{+,SBL}_{peak}$ along wall position $y^{+,SBL}$.

values obtained from data used in Figure-12. Thanks to the spatial resolution of the present SPIV system used for measurement, the relative error of peak location determination varies between $\pm 6.5^{+}$ to $\pm 18.2^{+}$ depending on the reference $\mathrm{Re}_{\theta,SBL}$ from smaller to largest. Each color represent the blowing ratio whereas symbols present particular Reynolds number at SBL. Outer peak of RMS streamwise fluctuation therefore, not only increased in magnitude but also move away from the wall with blowing ratio.

Similarly, outer peak of total turbulence kinetic energy $k^{+,SBL}_{peak}$ along corresponding wall location is presented in Figure-14 (b). The outer peak of $k^{+,SBL}_{peak}$ follow the same trend as for the outer peak of streamwise component, but with location slightly closer to the wall.

$$\frac{\sqrt{\overline{u'^2}}}{\overline{u}} = a + b(1 - \frac{\overline{u}}{U_\infty}) \tag{9}$$

In order to have a better understanding of the outer peak enhancement by blowing, Figure-16 shows $\sqrt{\overline{u'^2}}/\bar{u}$ plotted against $\bar{u}/U_\infty$. This plot can effectively remove the biased effect of wall friction and only the PIV calibration error is the source of error. In such a plot streamwise turbulence intensity scales linearly independent of the Reynolds number for SBL flows. Dotted gray line corresponds to Equation-9 (Alfredsson et al. (2011)) where a large part of the log and wake region collapses linearly at $\bar{u}/U_\infty$ between 0.6 and 0.9. A least square fit to the available data from XY plane for SBL conditions did allow us to determine the values of the empirical constants where, a = 0.287 and b = -0.259 which is slightly deviated from Alfredsson et al. (2011) (e.g a=0.286 and b=-0.255). Therefore, SBL data points from the present experiment and reference HWA data from Eitel-Amor (2014) collapse well to the linear relationship from Equation-9.

As stated in the description of the figure, markers with different color represent variations in the blowing. Therefore, increased deviation of the data from Equation-9 as a result of increased magnitude of blowing is observed. Remarkably data collapses well for each blowing ratio independent of the Reynolds number. Therefore, colored dash-dotted lines present a 5^{th} order fitting function to data of blowing. There colors have been chosen as same as the blowing ratio applied to the corresponding data set. In order to have better insight to the deviation from Equation-9, outer region is

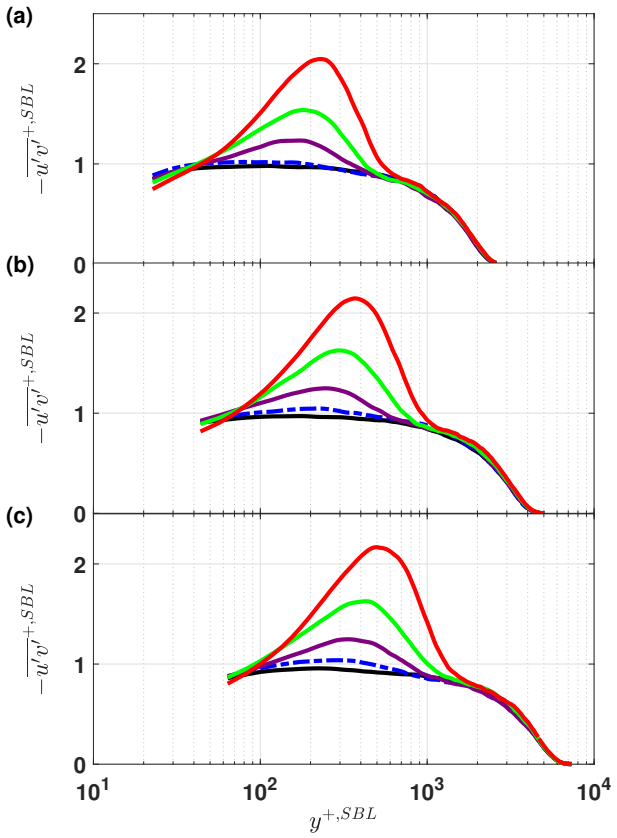

Figure 15.: RSS profiles for the different blowing ratio and Reynolds numbers normalised with inner variables of corresponding reference case, (a) at $\mathrm{Re}_{\theta,SBL} = 7500$,(b) at $\mathrm{Re}_{\theta,SBL} = 12500$ and (c) at $\mathrm{Re}_{\theta,SBL} = 18100$. Different colors of the profiles indicate different F as indicated in Figure-10 (a).

highlighted through the inset figure. Outer layer started deviating from Equation-9 at $[\sqrt{\overline{u'^2}}/\bar{u}, \bar{u}/U_\infty] = [0.925, 0.065]$.

Figure-15 shows the profiles of RSS for all investigated case using the similar inner scaling as Figure-10 (a). It is observed that a certain part of the outer region is enhanced with a clear outer peak as for all the turbulence intensity components. This peak is getting larger and stronger with increased blowing ratio. The peak value is also shifted away from the wall normal direction as F increases. This enhanced region is also moving with Reynolds number away from the wall. Finally, the profiles merged with their reference SBL data is earlier than predicted by Kametani and Fukagata (2011) who predicted that the full boundary layer is affected. DNS results from this literature described the behaviour of Reynolds shear stress (RSS) that increases with the blowing ratio e.g. in other words, RSS shifted away from the wall and the shifting of the RSS profiles persisted at edge of the boundary layer.

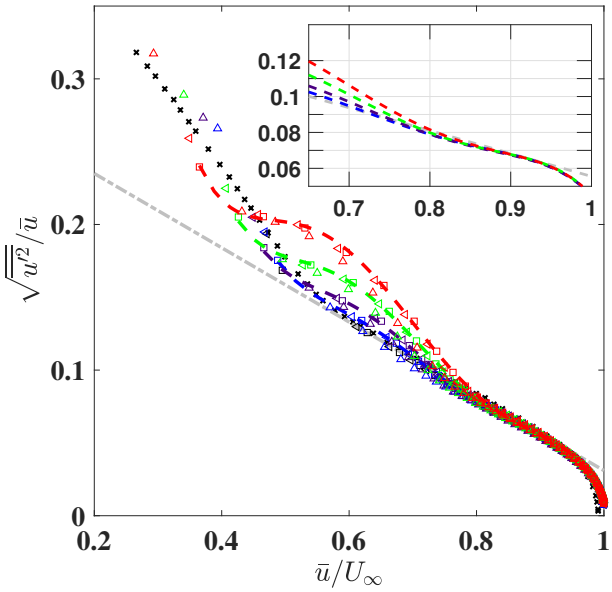

Figure 16.: RMS of streamwise turbulence intensity ($\sqrt{\overline{u'^2}}$) normalized with the local mean streamwise velocity is presented ($\bar{u}$) as a function of $\bar{u}/U_\infty$ after Alfredsson et al. (2011). Here SPIV data from XY plane is presented with hollow markers e.g. △: $\mathrm{Re}_{\theta,SBL} = 7500$; ◁: $\mathrm{Re}_{\theta,SBL} = 12500$ and □: $\mathrm{Re}_{\theta,SBL} = 18100$, '×': HWA data from Eitel-Amor (2014) at $\mathrm{Re}_\theta = 6335$. Different colors indicate variations in blowing ratios where, black symbols represent SBL conditions, blue, violet, green and red represent blowing ratios 0,1,3 and 6% respectively. '–.–' indicate Equation-9, '-.-', '-.-', '-.-' and '-.-' indicate a 5^{th} order fitting function. Inset figure highlight the region of the intersection of the fitted lines. One out of every 10 data points has been plotted in order to have better clarity.

On the contrary, viscous shear stress (VSS) profiles are reduced or shifted towards the wall. This phenomena was described as 'counterintuitive'. Although, present measurements are to be found consisted with first part of their findings albeit partially.

In the behavior of the VSS ($(\partial U/\partial y)^{+,SBL}$) profiles presented in Figure-17, a similar trend in the inner region is observed compared to the results of Kametani and Fukagata (2011) with a decrease of its intensity. However, the trend is opposite in the outer region where the VSS is enhanced. LES data from Eitel-Amor (2014) at $\mathrm{Re}_\theta = 7603$ is also presented in Figure-17 (a) as reference for SBL data which shows a perfect agreement. Although difference in the outer region is not much distinctive, therefore a separate plot within each figure is added to highlight the outer region. At all Reynolds number, VSS exhibit a clear peak at highest blowing fraction (F = 6%).

Figure-18 (a), 18 (c) and 18 (e) shows the profiles of the main production term in inner scale for all three Reynolds number respectively. Outer region is magnified using a separate plot within the main figure where in can be seen that blowing gradually increases the turbulence production. It is observed that inner and outer region is mostly unaffected while production is maximum within logarithmic region. This is even more prominent in pre-multiplied form used in Figure-18 (b), 18 (d) and 18 (f) which clearly exhibit a peak at all blowing cases. This peak is located within $10^2 < y^{+,SBL} < 10^3$ for all three Reynolds number.

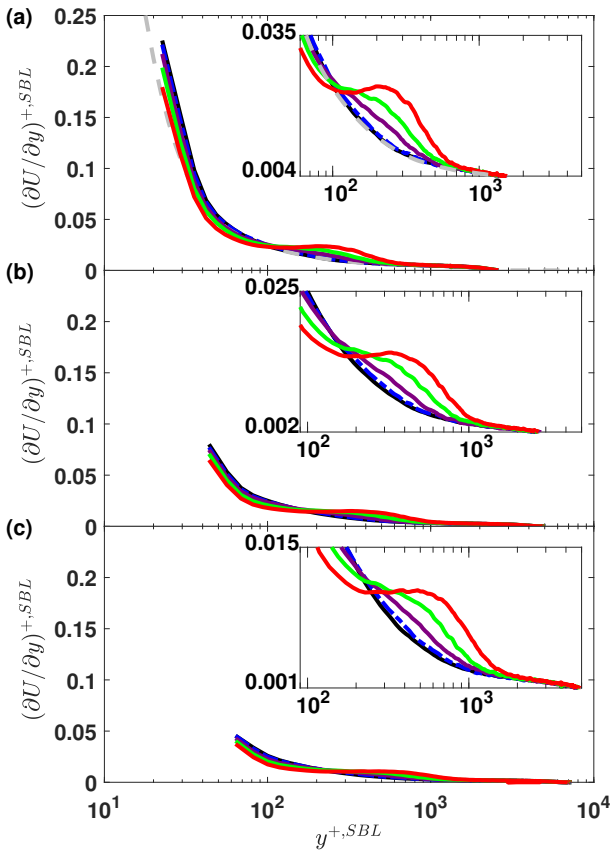

Figure 17.: Profiles of VSS plotted along normalized wall normal distance, different colors indicate blowing ratios in the same manner as Figure-10 (a) at $\mathrm{Re}_{\theta,SBL} = 7500$, here, '- - - - -' presents the LES data from Eitel-Amor (2014) at $\mathrm{Re}_{\theta} = 7603$, (b) at $\mathrm{Re}_{\theta,SBL} = 12500$ and (c) at $\mathrm{Re}_{\theta,SBL} = 18100$.

Figure-19 (a), (c) and (e) display the skewness profiles for $\mathrm{Re}_{\theta,SBL} = 7500$, 12500 and 18100 respectively and kurtosis profiles are plotted in Figure-19(b), (d) and (f). Blowing induced profiles vary different than that of SBL cases. The skewness varies in the wall normal direction in the log layer from positive values to negative ones for all cases with positive values and negative ones that increase and decrease respectively with blowing ratio. For the maximum blowing ratio investigated, it varies from 1/2 to -1/2. Finally, all skewness profiles merge to the outer region irrespective of their blowing ratios at certain Reynolds number. On the kurtosis side, similar effects of blowing are observed except the variation is opposite, i.e. Kurtosis first decreases with blowing close to the wall and then increases before merging to each other for all cases in the outer part.

Figure-20 is plotted in order to look into the pre-multiplied streamwise energy spectrum in the wave number space at $y^{+,SBL} \approx 250$. This is obtained using SPIV measurements following Foucaut et al. (2004). In general, spectral energy increases with increasing blowing ratio. It should be firstly noted that the high wave number range are poluted by noise and the transfert function of PIV (Foucaut et al. (2004)). However, an increase of the pre-multiplied spectrum in this range with blowing ratio for all Reynolds number investigated can be attributed preferentially to an increase of PIV noise probably linked with more out of plane motion due to blowing or by dilution

of the seeding concentration of particles by the unseeding air of the perforated plate. Blowing increases the pre-multiplied spectrum at small wave number so the energy contained into large scale structures. Of course, according to the energy cascade, the energy at higher wave number are also enhanced with blowing ratio. Effect of roughness between smooth and perforated plate is found to be small even if the large scale ranges are slightly enhanced.

8. Conclusion

We have conducted a series of SPIV measurement in a streamwise wall normal plane from a spatially developed turbulent boundary layer manipulated with micro-blowing device. For that a part of the smooth wall condition was replaced with a permeable surface and wall normal blowing was applied for blowing ratio F = 0 $\sim$ 6 %.

In light of the above mentioned results presented we can summarize the results of the present paper in the following categories;

(a) Boundary layer data without blowing was compared with the LES data from Eitel-Amor (2014) for validating the quality of the SPIV experimental set-up. A very good agreement was found between measured data and the reference LES data upto 4^{th} order moment.

(b) The microblowing strongly affect the boundary layer parameter. The momentum thickness and the shape factor are found to increase with blowing ratio. Blowing strongly influence first, second, third and fourth order statistical moments of the streamwise, wall normal and spanwise component of the velocity. Up to fourth order statistical moments for streamwise velocity, up to second order moment for spanwise and wall normal components is presented here for the present study. Blowing strongly affect the near wall region of the mean streamwise profile and enhances the turbulence intensity for all three velocity components with an outer peak which is increasing with blowing and moving away from the wall for all components. Ploting $\sqrt{\overline{u'^2}}/\bar{u}$ versus $\bar{u}/U_\infty$ shows interestingly no Reynolds number dependance at fixed blowing ratio. A fifth order function was fitted on the universal curves obtained at fixed blowing ratio.

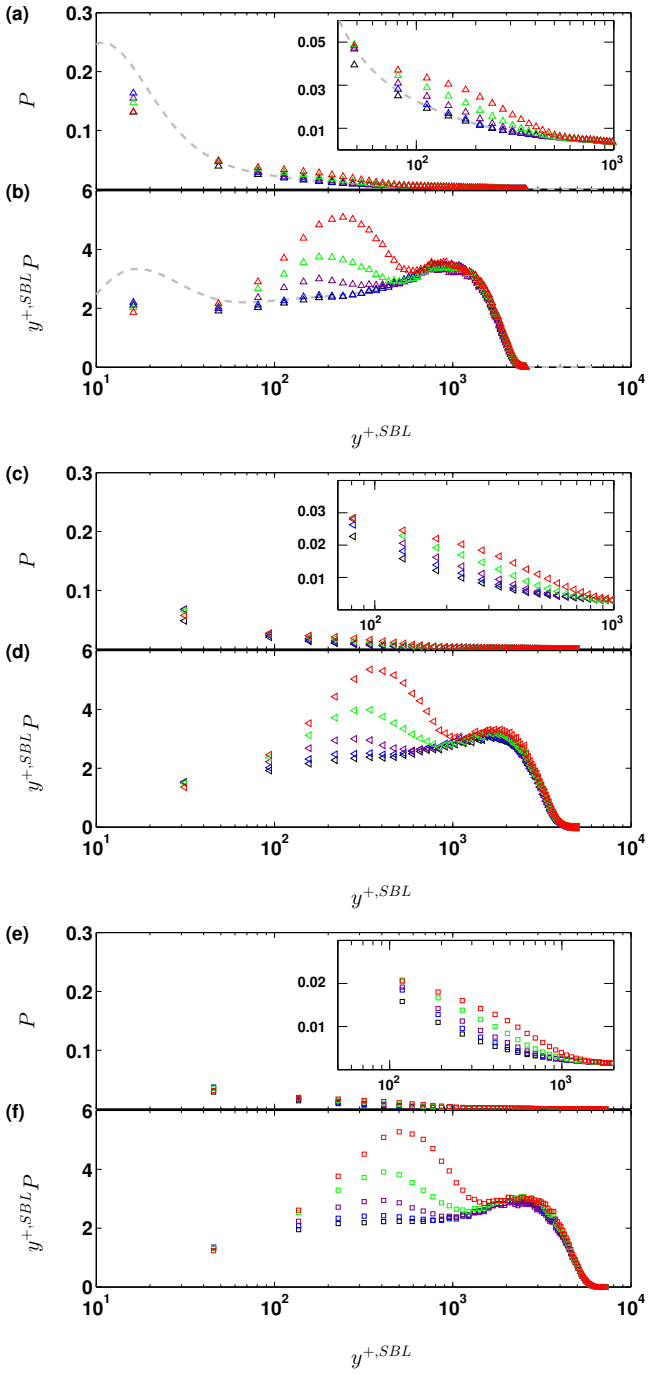

Figure 18.: Profiles of turbulent production term (P) and Pre-multiplied production ($y^{+,SBL}P$) along wall locations normalized with SBL inner parameter ($y^{+,SBL}$). '△'; (a) and (b) turbulent production term and Pre-multiplied production at $Re_{\theta,SBL} = 7500$ respectively, where gray 'dashed' line indicate data from Eitel-Amor (2014) at $Re_\theta = 7603$. '◁'; (c) and (d) turbulent production term and Pre-multiplied production at $Re_{\theta,SBL} = 12500$ respectively; '□'; (e) and (f) turbulent production term and Pre-multiplied production at $Re_{\theta,SBL} = 18100$ respectively. For different blowing ratios, color indication is similar to Figure-17, One out of every 5 data points have been plotted in order to have better visualization.

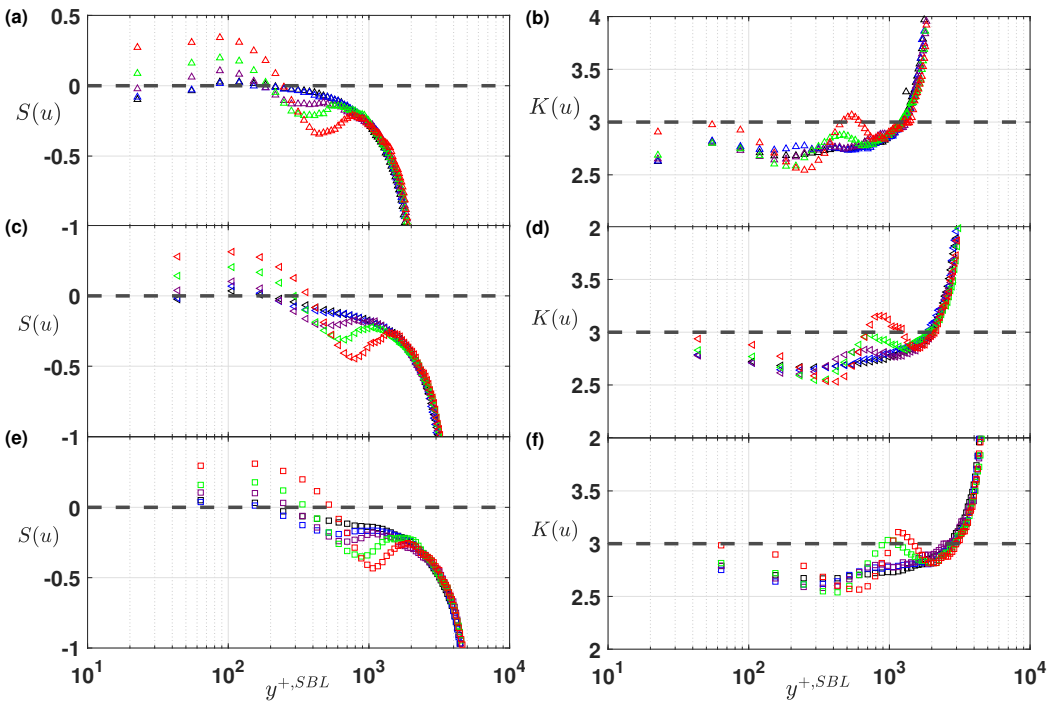

Figure 19.: Profiles of skewness (left column) and kurtosis (right column) of streamwise velocity component (u) along wall normal locations using inner co-ordinates obtained from corresponding SBL condition, '△'; (a) and (b) skewness and kurtosis at $\mathrm{Re}_{\theta,SBL} = 7500$ respectively, '◁'; (c) and (d) skewness and kurtosis at $\mathrm{Re}_{\theta,SBL} = 12500$ respectively, '□'; (e) and (f) skewness and kurtosis at $\mathrm{Re}_{\theta,SBL} = 18100$ respectively. Black symbols represent SBL conditions, blue, violet, green and red represent blowing ratios at 0,1,3 and 6% respectively. One out of every five data points are plotted for clarity.

(c) Being an active flow control technique, blowing use external energy injected into the flow field, this additional energy effects Reynolds shear stress and Viscous shear stress, eventually lead to an increased production of TKE. When plotting the production term in pre-multiplied form show that the production is enhanced with blowing in the logarithmic part with a clear peak.

(g) The spectra of steramwise velocity indicates an increase in energy with blowing ratio for low wave number at all three Reynolds number investigated in the present experiment.

Present paper has been written focusing in to the statistical perspective of a turbulent boundary layer under the influence of blowing at different ratios. Measurements from time resolved data with good spatial resolution in spanwise wall normal plane from the same experiment is obtained and currently under analysis. Therefore second part of the present experiment is intended to apply 'frozen turbulence hypothesis' from Taylor and 'attached eddy model' from Townsend and Perry in order to investigate the large scale influence in the log and outer region.

9. Acknowledgement

The authors of the present paper would like to acknowledge the financial support of the "European High performance Infrastructures in Turbulence (EuHIT)" project in the frame of its Transnational Access activity. This is a Project coordinated by Max Plank Institute Göttingen and funded by the European Commission under Grant agreement no: 312778, in the frame of the Research Infrastructures Integrating Activity (framework of FP7-INFRASTRUCTURES-2012-1). In particular Dr.-Ing. habil. Holger Nobach for his financial and organizational guidance. The visiting team would like to acknowledge the strong support and friendly atmosphere provided by the Laboratoire de Mécanique des Fluides de Lille (LMFL) group during the whole test campaign. Data presented in this paper can accessed through the following link:
`https://turbase.cineca.it/init/routes/#/logging/view_dataset/82/tabmeta`

The LMFL equipment used in this presented paper (the wind-tunnel, the PIV equipment and the compressed air regulation and quantification circuit) was funded by the ELSAT2020 project supported by the European Community, the French Ministry of Higher Education and Research and the Hauts de France Regional Council, in the framework of the CNRS Research Foundation on Ground Transport and Mobility.

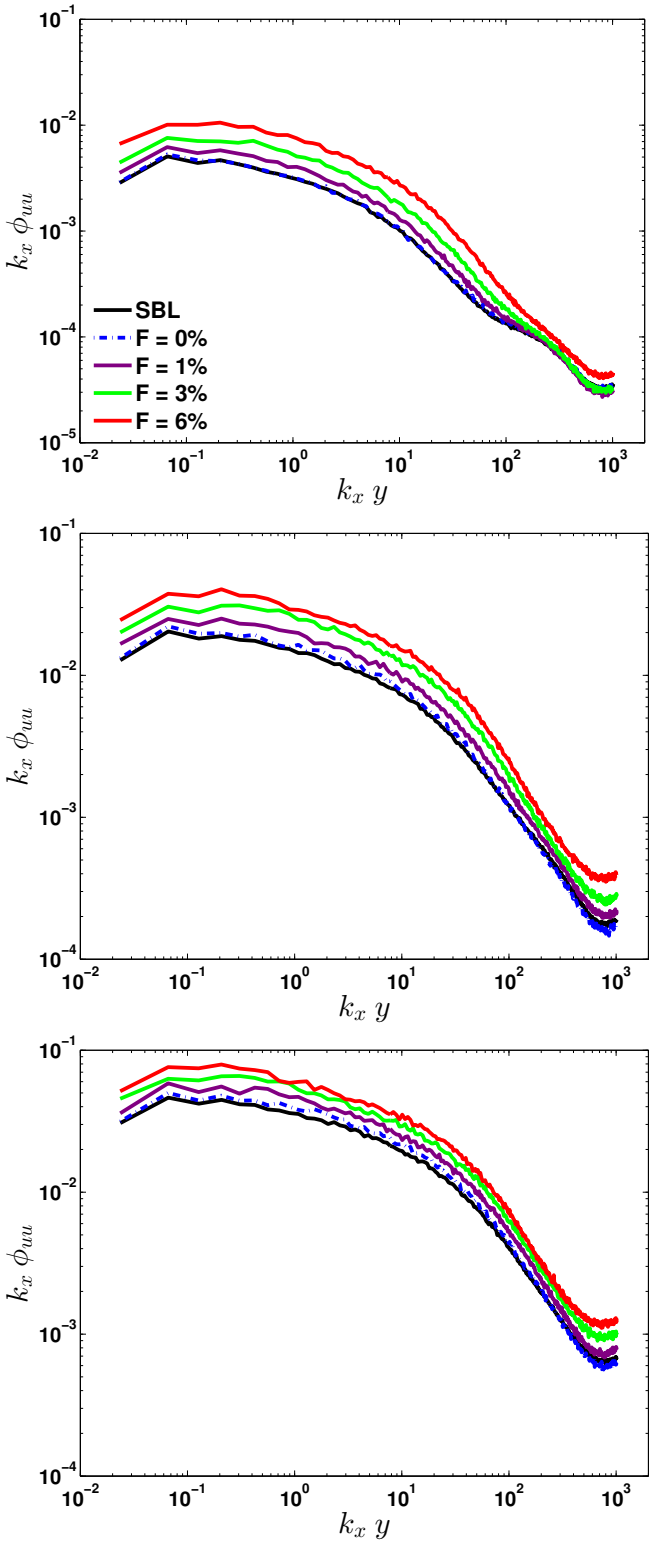

Figure 20.: Pre-multiplied streamwise energy spectrum along wall scaled wave number space. (Top) $\mathrm{Re}_{\theta,SBL} = 7495$, (Middle) $\mathrm{Re}_{\theta,SBL} = 12542$ and (Bottom) $\mathrm{Re}_{\theta,SBL} = 18094$.

References

Airbus Press Release. Airbus "BLADE" laminar flow wing demonstrator makes first flight. web site **https://www.airbus.com/newsroom/press-releases/en/2017/09/airbus-blade-laminar-flow-wing-demonstrator-makes-first-figh.html**, 2020, (January 1)

Anders, J., (1989). *LEBU drag reduction in high Reynolds number boundary layers. 2nd Shear Flow Conference*, *March 13-16*, Tempe, AZ, U.S.A., 1 – 10.

Abbassi, M. R.,Baars, W. J., Hutchins N. and Marusic I., (2017). *Skin-friction drag reduction in a high-Reynolds-number turbulent boundary layer via real-time control of large-scale structures. Int. Jour. Heat and Fluid Flow*, *67*, 30 — 41.

Alfredsson, P. H. and Örlü, R., (2010). *The diagnostic plot–a litmus test for wall bounded turbulence data. Eur. J. Mech. B/Fluids*, *29*, 403 -– 406.

Alfredsson, P. H., Segalini, A. and Örlü, R., (2011). *A new scaling for the streamwise turbulence intensity in wall-bounded turbulent flows and what it tells us about the "outer" peak. Phys. Fluids*, *23*, 041702.1 -– 4.

Ahn, S. and Fessler J., A., (2003). *Standard errors of mean. Variance and standard deviation estimators.* `http://web.eecs.umich.edu/~fessler/papers/files/tr/stderr.pdf`. Phil. Trans. R. Soc. A (2007) 365, 665–681

Balakumar, B., J. and Adrian, R., J. (2007). *Large- and very-large-scale motions in channel and boundary-layer flow.Phil. Trans. R. Soc. A*, *365* , 665 -– 681.

Blackwelder, R., F. (1989). *Some Ideas on the Control of Near-Wall Eddies.AIAA 2nd Shear Flow Conference*, *March 13-16* , Tempe, AZ, 1 -– 11.

Banister, D., Anderton, K., Bonilla, D., Givoni, M. and Schwanen, T. (2011). *Transportation and the environment.Annu. Rev. Environ. Resour.*, *36* , 247 -– 270.

Benedict, L., H. and Gould, R. D. (1996). *Towards better uncertainty estimates for turbulence statistics.Exp. Fluids*, *22(2)* , 129 – 136.

Bushnell, D. M. and Tuttle, M. H., (1979). *Survey and bibliography on attainment of laminar flow control in air using pressure gradient and suction. NASA*, *RP – 1035.*

Bushnell, D. M., (1983). *Turbulent Drag Reduction for External Flows. AIAA*, AIAA 21st Aero. Sci Meeting, Reno, Nevada, USA.

Bushnell, D. M., (2003). *Aircraft drag reduction: a review. Jour. Aero. Eng.:25th Anneversary Collection*, *217*, 1, 1 – 18.

Brasslow, A. L., (1999). *A History of Suction-Type Laminar-Flow Control with Emphasis on Flight Research. Monographs in Aerospace History*, *13.*

Benzi, R., (2010). *A short review on drag reduction by polymers in wall bounded turbulence. Physica D*, *239*, 1338 -– 1345.

Corda, S., (2017) *Introduction to aerospace engineering with a flight test perspective. Wiley*, *ISBN:9781118953365* , 1–928.

Choi, K.-S., (2001) *Turbulent Drag-Reduction Mechanisms: Strategies for Turbulence Management. Springer–Verlag, Vienna*, *415* , 161–212.

Choi K.-S. Jukes T. and Whalley R., (2001). *Turbulent boundary-layer control with plasma actuators. Phil. Trans. R. Soc. A*, *369*, 1443 — 1458.

Chin, C., Örlu, R., Monty, J., Hutchins, N., Ooi, A. and Schlatter, P., (2017). *Simulation of a Large-Eddy-Break-up Device (LEBU) in a Moderate Reynolds Number Turbulent Boundary Layer. Flow Turb. Combust.*, *98*, 445 – 460.

Corke, T. C., Guezennec, Y. and Nagib, H. M., (1981). *Modification in drag of turbulent boundary layers resulting from manipulation of large-scale structures. NASA CR 3444*, 1 – 25.

Carlier, J. and Stanislas, M., (2005) *Experimental study of eddy structures in a turbulent boundary layer using particle image velocimetry. J. Fluid Mech.*, *535*, 143 -– 188.

Coudert, S. and Schon, J., P., (2001). *Back-projection algorithm with misalignment corrections for 2D3C stereoscopic PIV. Meas. Sci. and Technol.*, *12*, 1371 – 1381.

Cuvier, C., (2012). *Active control of a separated turbulent boundary layer in adverse pressure gradient. PhD Thesis*, Ecole Centrale de Lille, 96.

Cuvier, C., Srinath, S., Stanislas, M., Foucaut, J., M., Laval, J., P., Kähler, C. J., Hain, R., Scharnowski, S., Schröder, A., Geisler, R., Agocs, J. , Röse, A., Willert, C., Klinner, J., Amili, O., Atkinson, C. and Soria, J., (2017). *Extensive characterisation of a high Reynolds number decelerating boundary layer using advanced optical metrology. Jour. Turb.*, 18:10, DOI: 10.1080/14685248.2017.1342827, 929 – 972.

Del Alamo, J. C., Jiménez, J., Zandonaze. P. and Moser. R. (2004). *Scaling of the energy spectra of turbulent channels. 30th Fluid Dynamics Conference*,Norfolk, Virginia, 39 – 56.

Dixon, W. J. and Massey, F. J. (1957). *Introduction to statistical analysis. MacGraw Hill.*

Eitel-Amor, G., (2014). *Simulation and validation of a spatially evolving turbulent boundary layer up to Re_θ=8300. Int. Jour. of Heat and Fluid Flow, 47*, 57 – 69.

Fukagata, K., Iwamoto, K. and Kasagi, N., (2002). *Contribution of Reynolds stress distribution to the skin friction in wall-bounded flows. Phys. Fluids, 14*, L73 – L76.

Foucaut, J-M., Carlier, J. and Stanislas, M. (2004). *PIV optimization for the study of turbulent flow using spectral analysis. Meas. Sci. and Technol., 15*, 1046 – 1058.

Foucaut, J-M., Coudert, S., Stanislas, M. and Delville J. (2010). *Full 3D correlation tensor computed from double field stereoscopic PIV in a high Reynolds number turbulent boundary layer. Meas. Sci. and Technol., 50*, 839 – 846.

Foucaut, J-M., Coudert, S., Braud C. and Velte C. (2014). *Influence of light sheet separation on SPIV measurement in a large field spanwise plane. Exp. Fluids, 25*, 035304:1 – 035304:10.

Foucaut, J-M., Cuvier, C., Willert, C. and Soria, J. (2018). *Characterization of a high Reynolds number turbulent boundary layer by means of PIV. 5th International Conference on Experimental Fluid Mechanics (ICEFM)*, 372 – 377, 02.-04. Jul. 2018, Munich, Germany.

Gad-el-Haq, M., (2000). *Flow Control: Passive, Active, and Reactive Flow Management. Cambridge Uni. Press, New York, ISBN: 0-521-77006-8(hb).*

Gad-el-Haq, M., (1996) *Modern Developments in Flow Control (Review). American Soc. Mech. Eng., 49*, doi: 10.1115/1.3101931, 365–379.

Ganapathisubramani, B., Clemens, N. T. and Dolling, D. S. (2007). *Effects of upstream boundary layer on the unsteadiness of shock induced separation. J. Fluid Mech., 585*, 369 – 394.

García-Mayoral, R. and Jimenéz, J., (2011). *Drag reduction by riblets. Phil. Trans. R. Soc. A, 369*, 1412 -– 1427.

Grant, H., L., (1958). *The Large Eddies of Turbulent Motion. J. Fluid Mech., 4.*

Hellsten, M., (2002). *Drag-reducing surfactants. Jour. Surfactants and Detergents, 5*, 65 – 70.

Hutchins, N. and Marusic, I., (2007). *Large-scale influences in near-wall turbulence. Phil. Trans. R. Soc., 365*, 647 -– 664.

Hutchins, N. and Marusic, I., (2007). *Evidence of very long meandering features in the logarithmic region of turbulent boundary layers. J. Fluid Mech., 579*, 1 -– 28.

Hutchins, N., Nickels, T., B., Chong, M., S. and Marusic, I., (2007). *Hot-wire spatial resolution issues in wall-bounded turbulence. J. Fluid Mech., 635*, 103 -– 136.

Hwang, D., (2004). *Review of research into concept of the microblowing technique for turbulent skin friction reduction (Review). Prog. In Aerospace Sciences, 40*, 559 -– 575.

Herpin, S., Wong, C. Y., Stanislas, M. and Soria, J., (2008). *Stereoscopic PIV measurements of a turbulent boundary layer with a large spatial dynamic range. Exp. Fluids, 45*, 745 – 763.

Herpin, S., Stanislas, M., Foucaut, J-M. and Coudert, S., (2013). *Influence of the Reynolds number on the vortical structures in the logarithmic region of turbulent boundary layers. J. Fluid Mech., 716*, 5 -– 50.

Horn, M., Seitz, A. and Schneider, M., (2015). *Novel tailored skin single duct concept for HLFC fin application. 7TH EUROPEAN CONFERENCE FOR AERONAUTICS AND SPACE SCIENCES (EUCASS)*, 1 -– 11.

International Air Transport Association, (2017). *Fact sheet fuel December 2017.* Retrieved from http://www.iata.org/pressroom/facts-figures/fact-sheets/Documents/factsheet-fuel.pdf,(accessed 8 January 2018).

International Maritime Organization, (2015). *Third International Maritime Organization Greenhouse Gas Study 2014: Executive summery and final report,* Micropress Printers, Suffolk, UK.

Joslin, R. D., (1998). *Overview of laminar flow control (Review). NASA Tech. Rep.*, 1998-208707.

Andy, Ko, Leifsson, L. T., Schetz, J. A., Mason, W. H., Grossman, B. and Haftka, R. T., (2003). *MDO (Multidisciplinary Design Optimization) of a Blended-Wing-Body Transport Aircraft with Distributed Propulsion. AIAA's 3rd Annual Aviation Technology, Integration, and Operations (ATIO) Technical Conference*, AIAA-2003-6732, 17 – 19 November, Denver, Colorado, 1 – 11.

Kim J., (2003). *Control of turbulent boundary layers. Phys. Fluids*, *15*, 1093 — 1105.

Kim J. and Bewley T. R., (2007). *A Linear Systems Approach to Flow Control. Annu. Rev. Fluid Mech.*, *39*, 383 — 417.

Kasagi, N., Suzuki, Y. and Fukagata, K., (2009). *Microelectromechanical Systems–Based Feedback Control of Turbulence for Skin Friction Reduction. Annu. Rev. Fluid Mech.*, *41*, 231 – 251.

Kim, J. (2011). *Physics and control of wall turbulence for drag reduction. Phil. Trans. R. Soc. A.*, *369* , 1396 -– 1411.

Kornilov, V. I. and Boiko, A. V. (2012). *Efficiency of Air Microblowing Through Microperforated Wall for Flat Plate Drag Reduction. American Institute of Aeronautics and Astronautics*, *50*(3), 724 -– 732.

Kornilov, V. I., (2015). *Current state and prospects of researches on the control of turbulent boundary layer by air blowing (Review). Prog. in Aerospace Sciences*, *76*(2), 1 -– 23.

Kostas, J., Foucaut, J-M. and Stanislas, M. (2005). *Application of Double SPIV on the Near Wall Turbulence Structure of an Adverse Pressure Gradient Turbulent Boundary Layer. Proceedings of the 6th International Symposium on PIV*, *Pasadana*, CA.

Kähler, C. J., Scharnowski, S., and Cierpka, C., (2016). *Highly resolved experimental results of the separated flow in a channel with streamwise periodic constrictions. J. Fluid Mech.*, *796*, 257 – 284.doi:10.1017/jfm.2016.250

Kametani, J. and Fukagata, K., (2011). *Direct numerical simulation of spatially developing turbulent boundary layers with uniform blowing or suction. J. Fluid Mech.*, *681*, 154 – 172.

Kametani, J., Fukagata, K., Örlü, R. and Schlatter, P. (2015). *Effect of uniform blowing/suction in a turbulent boundary layer at moderate Reynolds number. Int. Jour. Heat and Fluid Flow*, *55*, 132 – 142.

Kametani, J., Fukagata, K., Örlü, R. and Schlatter, P. (2016). *Drag reduction in spatially developing turbulent boundary layers by spatially intermittent blowing at constant mass-flux. Jour. Turb.*, *17(10)*, 913 – 927.

Krishnan K. S. G. and Bertram O. *Assessment of a chamberless active HLFC system for the vertical tail plane of a mid-range transport aircraft*, *Deutscher Luft- und Raumfahrtkongress*, Doc ID 450080, 1-7, 2017.

Lissaman, P. B. S., (1983). *Low Reynolds number aerofoils. Ann. Rev. Fluid Mech.*, doi: 10.1146/annurev.fl.15.010183.001255, **15**: 223 – 239.

Liu, C. K., Kline, S. J. and Johnston, J. P., (1966). *An experimental study of turbulent boundary layers on rough walls. Thermoscience Div., Mech. Eng. Dept., Stanford Univ.,*, *Rep. MD-15.*

Legner, H., H., (1984). *A simple model for gas bubble drag reduction. Phys. Fluids*, *27*, 2788 – 2790.

Marusic, I., Talluru, K., M. and Hutchins, N. (2014). *Controlling the Large-Scale Motions in a Turbulent Boundary Layer. Y. Zhou et al. (eds.), Fluid-Structure-Sound Interactions and Control*, Springer-Verlag Berlin Heidelberg 2014, *27*, 17 – 26.

Mathis, R., Hutchins, N. and Marusic, I., (2009). *Large-scale amplitude modulation of the small-scale structures in turbulent boundary layers. Jour. Fluid Mech.*, *628*, 311 – 337.

Mathis, R., Marusic I. and Hutchins N. (2010). *Predictive model for wall-bounded turbulent flow.. Science*, *329*, 193 -– 196.

Merkle, C., L. and Deutsch, S., (2010). *Microbubble drag reduction. Frontiers in Experimental Fluid Mechanics*, Editor: M. Gad-el-Hak, *46*, 291 – 335.

Mahfoze, O. and Leizet S., (2017). *Skin-friction drag reduction in a channel flow with streamwise-aligned plasma actuators. Int. Jour. Heat and Fluid Flow*, *66*, 83 — 94.

Marusic, I., Mathis, R. and Hutchins, N., (2010a) *High Reynolds number effect in wall turbulence. Int. J. Heat Fluid Flow*, *31(3)*, 418 -– 428.

Marusic, I., McKeon, B. J., Monkewitz, P. A., Nagib, H. M., Smits, A. J., (2010b). *Wall-bounded turbulent flows at high Reynolds numbers: Recent advances and key issues. Phys. Fluids*, *22*, 065103.1 -– 24.

Österlund, J. M., Johansson. A., V., Nagib. H. M. and Hites. M. H. (1999). *Mean-flow characteristics of High Reynolds Number Turbulent Boundary Layers from Two Facilities. 30th Fluid Dynamics Conference*,Norfolk, Virginia, 39 – 56.

Panton, R., L., (2001). *Overview of the self-sustaining mechanisms of wall turbulence. Prog. Aero. Sci.*, *37*, 341 – 383.

Prasad, A., K., (2000). *Stereoscopic particle image velocimetry. Exp. Fluids*, *29*, 103 – 116.

Prasad, A., K. and Jensen, K., (1995). *Scheimpflug stereocamera for particle image velocimetry in liquid flows. Appl. Optics*, *34*, No-30, 7092 – 7099.

Plas, A. P., Sargeant, M. A., Madani, V., Crichton, D., Greitzer, E. M., Hynes, T. P. and Hall, C. A., (2007). *Performance of a Boundary Layer Ingesting (BLI)Propulsion System. 45th AIAA Aerospace Sciences Meeting and Exhibit*, AIAA 2007-450, 8 – 11 January, Reno, Nevada, 1 – 21.

Rothstein, J. P., (2010). *Slip on Super hydrophobic surfaces (Review). Annu. Rev. Fluid Mech.*, *42*, 89 -– 109.

Reneaux, J., (2004). *Overview on drag reduction technologies for civil transport aircraft. Meth. Appl. Sci. Eng.*, ECCOMAS 2004, Jyväskylä, 24—28 July 2004, 1 – 18.

Schlichting, H., (1979). *Boundary layer theory. McGraw-Hill*, New York.

Örlü, R. and Schlatter, P., (2015). *Comparison of experiments and simulations for zero pressure gradient turbulent boundary layers at moderate Reynolds numbers. Exp. Fluids*, *43*:1547, 1 – 21.

Smits, A. J., McKeon B. J., Marusic, I., (2011). *High Reynolds number wall turbulence. Annu. Rev. Fluid Mech.*, *43*, 353 – 375.

Schlichting, H., (1942a). *The boundary layer on a flat plate under conditions of suction and air injection (Die Grenzschicht an der ebenen Platte mit Absaugung und Ausblassen). Luftfahrtforschung*, *19*, 293 -– 301.

Spallart P. R. and McLean J. D., (2011). *Drag reduction: enticing turbulence, and then an industry (Review). Phil. Trans. R. Soc. A*, *369*, 1556 -– 1569.

Stroh A., Frohnapfel B., Schlatter P. and Hasegawa Y., (2015). *A comparison of opposition control in turbulent boundary layer and turbulent channel flow. Phys. Fluids*, *27*, 075101-1 — 075101-14.

Stroh, A., Hasegawa, Y., Schlatter, P. and Frohnapfel, B., (2016), *Global effect of local skin friction drag reduction in spatially developing turbulent boundary layer*, *J. Fluid Mech.*, 805, 303 – 321

Scarano, F., (2002). *Iterative image deformation methods in PIV. Meas. Sci. and Technol.*, *13*, R1 – R19.

Soria, J., Cater, J. and Kostas, J., (2000). *High resolution multigrid cross-correlation digital PIV measurements of a turbulent starting jet using half frame image shift film recording. Laser and Optics Tech.*, *31*, 1, 3 – 12.

Soria, J., (1996). *An investigation of the near wake of a circular cylinder using a video-based digital cross-correlation particle image velocimetry technique. Laser and Optics Tech.*, *31*, 12, 221 – 233.

Soloff, S. M., Adrian, R. J. and Liu, Z. C. (1997). *Distortion compensation for generalized stereoscopic particle image velocimetry. Meas. Sci. and Technol.*, *8*, 1441 – 1454.

Spalart, P.R., Strelets, M. and Travin, A., (2001). *Direct numerical simulation of large-eddy-break-up devices in a boundary layer. Phil. Trans. R. Soc. A*, *27*, *5*, 902 — 910.

Smith, L. H., (1993). *Wake Ingestion Propulsion Benefit. Jour. Propulsion Power*, *9*, No.1, 74 – 82.

Sciacchitano, A. and Wieneke, B. (2016). *PIV uncertainty propagation. Meas. Sci. Technol.*, *27*, 1 – 16,(doi:10.1088/0957-0233/27/8/084006).

Srinath, S., Vassilicos, J., C., Cuvier, C., Laval, J.-P., Stanislas, M. and Foucaut, J.-M. (2018). *Attached flow structure and streamwise energy spectra in a turbulent boundary layer. Phys. Rev. E*, *97(5)*, 1 – 14.

Tamano, S., Itoh, M., Kato, K. and Yokota, K., (2010). *Turbulent drag reduction in nonionic surfactant solutions. Phys. Fluids*, *22*, 055102.1 – 12.

Tang,, Z., Jiang, N., Zheng, X. and Wu, Y., (2019). *Local dynamic perturbation effects on amplitude modulation in turbulent boundary layer flow based on triple decomposition. Phys. Fluids*, *31(2)*, 025120.1 – 14.

Van Driest, E. R., (1956). *On turbulent flow near a wall. AIAA*, *23*:11, 1007 – 1011, 1036.

Vallikivi, M., Hultmark, M. and Smits A. J., (2015a). *Turbulent boundary layer statistics at very high Reynolds number. J. Fluid Mech.*, *779*, 371 – 389.

Vallikivi, M., Ganapathisubramani, B. and Smits A. J., (2015b). *Spectral scaling in boundary layers and pipes at very high Reynolds numbers. J. Fluid Mech.*, *771*, 303 – 326.

Vukoslavčević, P. Wallace, J., M. and Bailnt, J., L., (1991). *Viscous drag reductions using streamwise aligned riblets. AIAA*, *30*, 1119 -– 1125.

Warsop C. Current status and prospects for flow control. *Aerodynamic drag reduction technologies*, Springer-Verlag Berlin Heidelberg GmbH, **999**: 269-277, 2000.

Wood, R. M., (2004). *Impact of Advanced Aerodynamic Technology on Transportation Energy Consumption. SAE International 2004*, Technical Paper, *2004-01-1306.*.

Willert, C. J., (2015). *Experimental Evidence of Near-Wall Reverse Flow Events in a Zero Pressure Gradient Turbulent Boundary Layer. Phys. Fluid Dyn.*, 01 – 08 .

Wieneke, B. (2005). *Stereo-PIV using self-calibration on particle images. Exp. Fluids*, *39*, 267 – 280.

Westerweel, J., Dabiri, D. and Gharib, M., (2000). *The effect of a discrete window offset on the accuracy of cross-correlation analysis of digital PIV recordings. Exp. Fluids*, *23*, 1, 20 – 28.

Willert, C. A. and Gharib, M. (1991). *Digital particle image velocimetry. Exp. Fluids*, *10*, 181 – 193.

White, C. M. and Mungal, M. G., (2008). *Mechanics and Prediction of Turbulent Drag Reduction with Polymer Additives (Review). Annu. Rev. Fluid Mech.*, *40*, 235 – 256.

Walsh M.J. and Lindemann A.M., (1984). *Optimization and application of riblets for Turbulent Drag Reduction. AI AA-84-0347*, *22nd Aerospace Sciences Meeting*,Reno, Nevada, USA, *9-12 January*, 1 — 10.

Wilkinson, S. P., Anders, J. B., Lazos, B. S. and Bushnell, D. M., (1988). *Turbulent drag reduction research at NASA Langley: Progress and Plans. Int. J. Heat and Fluid Flow*, *9*, *3*, 266 — 277.

Zagarola, M. and Smits, A., J., (1998). *Mean-flow scaling of turbulent pipe flow. Jour. Fluid Mech.*, *373*, 33 — 79.